Electric Field/Current-Assisted Sintering of Optical Ceramics

16

Hidehiro Yoshida

Contents

H. Yoshida (✉)
Department of Materials Science, School of Engineering, The University of Tokyo, Tokyo, Japan
e-mail: hyoshida@material.t.u-tokyo.ac.jp

© Springer Nature Switzerland AG 2020

Y. R. Mahajan, R. Johnson (eds.), *Handbook of Advanced Ceramics and Composites*,
https://doi.org/10.1007/978-3-030-16347-1_19

Abstract

This chapter aims to provide an updated and comprehensive description of the development of electric field/current-assisted sintering (ECAS) technique for the production of dense, structural/functional ceramics, particularly transparent polycrystalline ceramics. ECAS is gaining interest in recent decades due to the accelerated consolidation compared to conventional, pressureless sintering and pressure-assisted sintering (such as hot-pressing). In particular, spark plasma sintering (SPS) or pulsed electric current-assisted sintering (PECS), in which pulsed direct current is applied to directly heat up material under compressive stress, has been extensively studied as an extremely powerful tool. This process is capable of producing nanoceramics and transparent ceramics in a relatively short sintering time and low sintering temperature, being promoted for practical use. The short sintering time and low sintering temperature are in fact desirable for attaining high transparency and excellent mechanical properties for polycrystalline materials.

ECAS process is still drastically improving with new findings and technologies being actively reported. For instance, flash sintering, where densification occurs almost immediately (typically <5 s) under strong electric field, has been developed in recent decade and has been attracting extensive attention as an innovative sintering technique. In this chapter, the earlier experimental works on SPS methods and characteristic properties of the produced transparent materials are summarized, and recent attempts for elucidation of the underlying mechanisms responsible for the SPS are briefly introduced.

Keywords

Electric current · Electric field · Electric current-assisted sintering · Spark plasma sintering · Oxide ceramics · Densification · Grain size · Mechanical strength

Abbreviations

3Y-TZP	3 mol% yttria-stabilized tetragonal zirconia polycrystal
DC	Direct current
ECAS	Electric field/current-assisted sintering technique
EELS	Electron energy loss spectrometry
HA	Hydroxyapatite, $Ca_{10}(PO_4)_6(OH)_2$
HIP	Hot isostatic pressing
HP	Hot pressing
IR	Infrared
PECS	Pulsed electric current-assisted sintering
SPS	Spark plasma sintering
TEOS	Tetraethyl orthosilicate
YAG	Yttrium aluminum garnet, $Y_3Al_5O_{12}$
YSZ	Y_2O_3-stabilized ZrO_2

Introduction

Common optically transparent materials, such as glasses and polymers, have been widely used in industrial applications and daily life. However, these materials have relatively poor mechanical strengths and sometimes insufficient chemical and physical stabilities. Also, they usually possess relatively low melting temperatures and low resistance against corrosive atmosphere, so that they cannot be used for applications at high temperatures or other harsh environment. Ceramic materials therefore emerge as a powerful candidate for transparent materials used in high temperature and/or corrosive environments. Single crystals of ceramics, such as sapphire (Al_2O_3) and YAG ($Y_3Al_5O_{12}$), are essentially optically transparent and have been actually in practical use for various industrial applications. However, growth of single crystals requires very high temperature and long processing time, leading to expensive products and components. Hence, transparent polycrystalline ceramics are of practical importance in the field of optical applications. The advantage of polycrystals is that they can be larger in dimensions and can be produced at lower temperatures, comparing to single crystals. In addition, functionalization of ceramic body by doping or manufacturing functionally graded materials can be more easily prepared for polycrystalline ceramics than single crystals. In contrast to single crystals, polycrystalline ceramics are in general opaque, because of the presence of light-scattering sources as mentioned later. In order to attain optical transparency in polycrystalline ceramics, it is necessary to eliminate residual pores and other defects from sintered body, because the presence of such defects drastically deteriorates optical quality.

A number of efforts have been made to eliminate residual defects from sintered bodies by various synthesis methods so far. Improving sinterability is essential to minimize defects (residual pores in sintered body), leading to optical transparent ceramics, so that researchers have optimized sintering conditions from raw powder synthesis to consolidation methods. As for sintering processes, pressure-assisted techniques such as hot-pressing (HP) and hot isostatic pressing (HIP) are widely employed to improve the quality of sintered materials and to fabricate transparent ceramic bodies. HIP synthesis, in fact, is an effective technique to produce transparent bulk ceramic body.

Among pressure-assisted sintering, spark plasma sintering (SPS), also known as electric field/current-assisted sintering technique (ECAS) or pulsed electric current-assisted sintering (PECS) method, has attracted considerable attention as a short-time and low-temperature synthesis method for production of transparent ceramics. SPS is a solid compressive and pulsed electric-current-energizing sintering method. In recent decades, owing to the remarkable development of SPS machines and techniques, a considerable number of studies were performed to produce high-performance ceramics by ECAS/SPS. SPS is also capable of producing highly dense and nanostructured sintered compacts, even in case of ceramics with poor sinterability. Recently, SPS has proved to be a powerful method to manufacture transparent polycrystalline ceramics. In addition, power consumption of the SPS synthesis is about one-third to one fifth of that of traditional techniques, including normal pressureless sintering, HP, and HIP [1, 2].

SPS takes advantage of both high applied currents and mechanical pressure to deliver significantly higher densification rates than conventional pressureless sintering or HP [1]. In fact, several advantages over conventional sintering techniques are provided by SPS for fabricating transparent ceramics. In addition, new technologies regarding ECAS processes are still being reported actively, to promote low-temperature and short-time consolidation of powder compacts. Also, mechanisms underlying ECAS and SPS are being enthusiastically investigated. This chapter aims to briefly summarize ECAS and SPS techniques and to cover transparent oxide ceramic materials produced by SPS. Also, several new attempts of ECAS to enhance full densification of ceramic materials are introduced.

Role of Microstructure on Optical Properties

It has been widely accepted that the microstructure of polycrystalline ceramics plays a key role in their optical properties. It is beneficial to briefly summarize important microstructural features which determine optical transparency for visible and near-infrared (IR) wavelength in polycrystalline ceramic materials. Owing to wide bandgap of common ceramic materials, ceramic single crystal is essentially transparent for visible and IR wavelength. However, polycrystalline ceramics are generally opaque, due to the presence of various light-scattering factors.

The critical factors which determine optical transparency in ceramics are refractive index of crystals (i.e., isotropy of crystal structures), grain boundaries and interfaces, and porosity of polycrystalline body. For attainment of optical transparency in polycrystalline ceramics, isotropic, high symmetry of the crystals, i.e., similar refractive index in all directions, is preferable. Cubic symmetry is therefore an ideal crystalline structure for transparency. But, the dominant microstructural feature that sensitively influences transparency is porosity. Residual pores in sintered ceramic bodies degrade transparency of the materials due to scattering of light at the pores. The refractive index significantly different between material and ore, resulting in reflection and refraction of light [2, 3].

It has been widely accepted that the in-line transmission should increase with the increasing grain size, because the increased number of grain boundaries gains light-scattering source. In fact, optical scattering decreases with the increasing grain size and with decreasing the number of the grain boundaries in fully densified Al_2O_3 polycrystals with the grain size beyond 20 μm, the size of which is much larger than the wavelength of visible light [4]. However, recent investigations have revealed that the contribution of grain boundaries to scattering is rather small in oxide polycrystals with submicron grain sizes [5–8]. Hayashi et al. examined transmission optical properties of HIPed Al_2O_3 polycrystals with the average grain size in a range of 0.82–1.43 μm [5] and confirmed that the transmission monotonically increases with the decreasing average grain size.

Important microstructural features and their interaction with visible/IR radiation light are schematically described in Fig. 1 [2, 3]. Figure 1a illustrates polycrystalline ceramics with micrometer-sized grains and pores. In materials with pore sizes in the

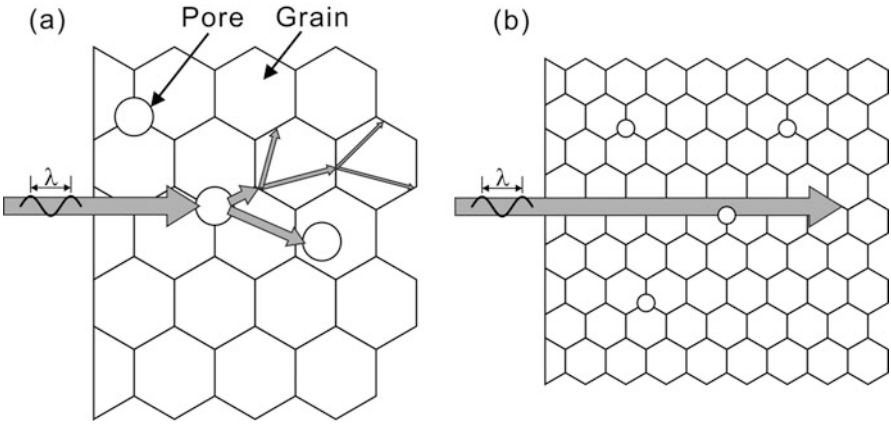

Fig. 1 Microstructure of polycrystalline ceramics and light transmission through the ceramics. (**a**) Polycrystalline ceramics with micrometer-sized grains and pores and (**b**) nanometer-sized grains

micrometer range (i.e., dimensions comparable to the wavelength of the light λ), pores significantly scatter light. In order to achieve high transparency in ceramics with micrometer-sized pores, the porosity must be reduced to much less than 0.1%. As mentioned above, when the pore sizes decrease to the nanometer range, their interaction with visible light becomes minimal, and the optical transparency increases. In addition, grain boundary is another scattering source because of anisotropic refractive indices of grains; light is refracted at each grain boundary since each grain in a random polycrystalline ceramic represents a discontinuity in refractive index. Taking these light-scattering sources into account, conventional transparent ceramics are developed by eliminating residual pores and by increasing grain sizes (i.e., decreasing number of grain boundaries). Compression sintering, such as HIP, is often employed to attain fully densified and large grain-sized microstructure; compressive stress effectively facilitates breaking agglomerated grains and eliminating residual intergranular pores.

Recent development on SPS methods allows fabrication of fully densified ceramic body consisting of ultrafine (submicron-sized) grains, in comparison to HP and HIP methods. In SPS, material temperature is raised by pulsed direct current (DC) applied through graphite die and punches, not by heating from outside die. The almost direct heating of material in SPS may allow densification at lower temperature in shorter holding time, compared with HP and HIP. As shown later, the characteristics of SPS contribute to enhance densification and to reduce grain sizes of sintered body. Hence, the strategy to attain the transparency of ceramics has been changed to full densification of nanocrystallized ceramics. Figure 1b illustrates an anisotropic material with grain sizes in nanocrystalline range. By reducing the grain size lower than the wave length of visible light, light is not scattered at grain boundaries [2, 3]. Furthermore, refinement of grain size is also advantageous to

improve mechanical strength of polycrystalline material. Production of transparent ceramics by means of SPS technique will be beneficial for industrial application in comparison to traditional HP or HIP processing.

Operating Principle of SPS

Basic Apparatus of SPS

A schematic of the typical apparatus of SPS is shown in Fig. 2a, together with an illustration of HP setup (Fig. 2b). In HP, the process of diffusion and/or plastic flow of powder compact is promoted by both heating from outside die and compressive stress; these two factors contribute to promote sintering densification. Due to the usage of graphite die in HP, the sintering is usually conducted in vacuum or inert gas (but thanks to the atmosphere, tungsten mesh heating elements can be used in the chamber).

ECAS/SPS machine also consists of a mechanical loading system, as well as HP, but the loading jigs act at the same time as electrodes, placed in a chamber under vacuum. The sintering of SPS is carried out in vacuum by using a graphite die, and compressive stress is applied to graphite punches, as well as conventional HP. But, the material is heated up by means of pulsed DC current, supplied by a patented power generator, applied through electrodes at the top and bottom of the graphite punches [9–11]. Owing to the high electrical conductivity of the materials used for dies and punches, low voltage is applied to the whole setup including material, die, and punches, to yield high current, leading to efficient Joule heating of the material.

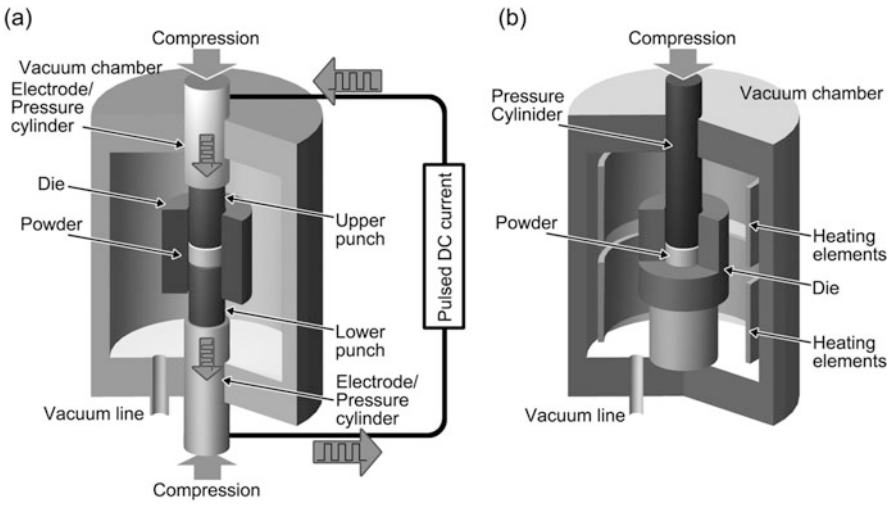

Fig. 2 A schematic of (**a**) typical apparatus of spark plasma sintering (SPS) machine and (**b**) hot-pressing (HP) setup

The typical voltage applied to the whole setup in SPS is usually in a range of 4–20 V. The average value of current is in a range of 500 A to 40 kA, depending on sintering conditions and electric conductivity of the material.

Because only die and punches are heated in SPS, heating rates can be in SPS of as high as several hundred degrees over a minute. Standard cooling rates up to 150 °C/min are usually employed; additional active cooling under gas flow enables to reach quenching rates of 400 °C/min. As a result, heating rate typically used is 20–200 °C/min, and much faster heating rate up to 1000 °C/min can be employed. Even in the case of electrically non-conductive raw powder, heat is quickly transferred to the material inside the die, owing to high thermal conductivity of the die and punches. SPS therefore enables to significantly reduce the total duration of the process and energy costs. Maximum temperature achieved by using standard graphite tools lies beyond 2000 °C. The pulsed DC current is automatically controlled to attain target temperature. The pulse and pause durations for SPS operation is typically in the order of a few milliseconds.

In the operation of ECAS/SPS, the control of temperature of die or punches during SPS, with heating rates of several hundreds of °C/min, is an important and critical matter; the SPS temperature must be monitored with high responsivity to control heating schedule. Main requirements for a reliable temperature measurement are a short reaction time and a high reproducibility. The temperature is usually measured by an optical pyrometer focused onto the surface of the die or the punches or by a thermocouple placed inside the die.

Attempts to measure the temperature of the material inside the die during SPS have been carried out so far. For instance, Misawa and co-workers measured the temperature of ZnO specimen as well as the internal current of the powder compact inside a graphite die during SPS process by using Pt electrodes and magnetic probe (coil), as schematically shown in Fig. 3 [12]. In the case of ZnO specimen, decrease of electric resistance was detected during sintering process. The initial current that

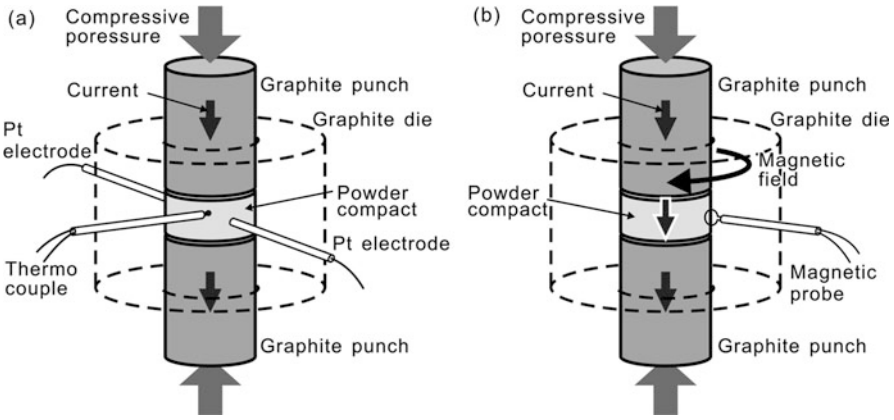

Fig. 3 Schematic of (**a**) temperature, electric resistance, and (**b**) magnetic field measurement system inside a graphite die during SPS processing [7]

flowed through the ZnO powder compact was several hundred amperes, and the ratio of the internal current through the specimen to the total current increased with the progress of densification. However, it is still technically difficult to directly measure the materials' temperature during SPS synthesis. Probably we need theoretical approach, such as finite element modeling (FEM), to estimate the material temperature. In particular, FEM is an important tool to predict the distribution of temperature, current, electrical potential, and stress that emerged during SPS process at the micro-, meso-, and macroscopic scales. FEM analysis has been widely employed for elucidation and controlling of specimen temperature and stress distribution developed in SPS operation. Detailed overview of calculation works is given by Orru et al. [13].

At the same time, the simultaneous application of a uniaxial mechanical pressure enhances densification as well as HP and HIP. The compressive stress is typically in a range of 20–100 MPa, but ultrahigh pressure of several hundred MPa–1 GPa can also be employed (for ultrahigh-pressure SPS, we need to use some special dies). Recently, pressure or displacement becomes another important controlling parameter for SPS operation.

Advantages of SPS are fast sintering process, suppressed grain growth, and single step compaction and sintering processes. However, SPS method has some disadvantages, particularly only simple symmetrical shapes and limited sizes being allowed in SPS synthesis. The drawbacks in SPS have always been pointed out as well as in HP, but at least enlarged dimensions of the sintered bodies have been gradually attained in recent years.

Mechanisms of Densification by SPS

SPS technique has a significant advantage over HP and HIP, because it can complete the powder consolidation within a short time duration [14]. SPS has a potential to densify nanosized powders without significant grain coarsening which is unavoidable during the conventional densification routes. The densification process in SPS is generally divided into three stages [15]. The first stage is characterized by the packing of raw particles, the second stage is a diffusional process including the neck formation and grain sliding, and the final stage is the removal of closed pores mainly through grain boundaries.

It was expected that electrical discharge plasma takes place between powder particles, resulting in localized and momentary heating of the particle surfaces [9]; self-heat generation by the electric discharge plasma between particles at an early stage of on-off DC pulse application would act on promoting sintering. In addition, it has been speculated that the surfaces of the particles are purified and activated due to the electric discharge plasma on the particle surfaces; the purified surface layers of the particles could melt and fuse to each other forming necks between the particles [10]. However, the occurrence of the discharge has been questioned in recent years.

It is widely accepted that electric field can accelerate densification of ceramics, while the primary purpose of imposed electric field/current in SPS is usually supposed to provide the required amount of resistive heating. For instance, DC electrical fields of approximately 20 V/cm lower the sintering temperature of 3 mol% yttria-stabilized tetragonal zirconia polycrystal (3Y-TZP) from 1400 °C to 1300 °C [16]. However, the origin of the electric field on the enhancement of mass transport is still unclear. In the case of SPS, the applied voltages are usually rather low, lower than the required value to trigger electromigration. Recently, it has been reported that electric field/current can involve formation of anion vacancies in ceramics [17]; electron energy loss spectrometry (EELS) analysis suggested that Y_2O_3 polycrystal consolidated by SPS exhibited reduced state in comparison to Y_2O_3 sintered in air and in vacuum. Highly reduced state in other oxide ceramics densified under strong electric field or current have also been revealed by EELS analysis, as mentioned later. The role of DC field and/or current is still an open question, but it would seem that field/current can trigger the formation of ionic defects and consequently facilitate diffusional mass transport, leading to acceleration of densification of ceramic materials.

Besides these electric field/current effects, the densification behavior in SPS can be quantitatively analyzed based on high-temperature mass transport rate equation. In the early stage of sintering, the temperature of the punches and die is raised prior to the heating of the compacted powder, due to low electric conductivity of the raw powders [18]. The temperature of the compact is gradually increased by the heating of the die and punches, and then the electric current through the compacted powder accordingly increases, resulting in Joule heating of the material [18]. An applied pressure strongly affects the initial packing and densification in the second and third stages. A high pressure is constantly applied in common SPS process. Heating rate is another important sintering parameter for densification in the second and third stages; high heating rate is supposed to be one of the strong advantages of SPS synthesis over HP and HIP. In SPS, specimen temperature can be raised in relatively short time, resulting in suppression of grain growth during the heating process of sintering.

Here, we take a look at an example of phenomenological analysis of the densification process in SPS [19]. Mass transport during sintering with or without an external load can be regarded as analogous to that occurring in high-temperature creep. The steady-state creep strain, ε, can be described by a general constitutive relationship where the creep rate is a minimum and remains at an almost constant value:

$$\frac{\mathrm{d}\varepsilon}{\mathrm{d}t} = \dot{\varepsilon} = A\frac{\phi\mu b}{kT}\left(\frac{b}{G}\right)^{\mathrm{p}}\left(\frac{\sigma}{\mu}\right)^{\mathrm{n}} \tag{1}$$

where $\dot{\varepsilon}$ is the creep rate, t the time, A a constant, ϕ the diffusion coefficient, μ the shear modulus, b the Burgers vector, k the Boltzmann's constant, T the absolute temperature, G the grain size, σ the macroscopic applied stress, and p and n the grain size and stress exponents, respectively. The HP kinetics can be written in a simplified

version by dropping the negligible small thermodynamic driving forces. The densification rate is then given by

$$\frac{1}{D}\frac{\mathrm{d}D}{\mathrm{d}t} = \frac{B\Phi\mu_{\mathrm{eff}}b}{kT}\left(\frac{b}{G}\right)^{\mathrm{p}}\left(\frac{\sigma_{\mathrm{eff}}}{\mu_{\mathrm{eff}}}\right)^{\mathrm{n}} \tag{2}$$

where D is the instantaneous relative density, B a constant, σ_{eff} the instantaneous effective stress acting on the powder compact, and μ_{eff} the instantaneous shear modulus of the powder compact. Taking into account the porosity dependence of the material's physical properties, Eq. (2) can be modified as

$$\frac{1}{\mu_{\mathrm{eff}}}\frac{1}{D}\frac{\mathrm{d}D}{\mathrm{d}t} = K\frac{\exp(-Q_{\mathrm{d}}/RT)}{T}\left(\frac{b}{G}\right)^{\mathrm{p}}\left(\frac{\sigma_{\mathrm{eff}}}{\mu_{\mathrm{eff}}}\right)^{\mathrm{n}} \tag{3}$$

Here $K = Bb\Phi_0/k$ is a constant (with Φ_0 the pre-exponential term of the diffusion coefficient) and Q_{d} the apparent activation energy for the mechanism which rate-controls densification. From Eq. (3), the parameters of p, n, and Q_{d} are experimentally determined, enabling the identification of the rate-controlling mechanisms of densification of the powder compact during SPS. For example, for diffusion-controlled densification, the strain rate is proportional to the effective stress ($n = 1$). Because densification process is a thermally activated process, densification is also characterized by the activation energy of the rate-controlling mechanism (grain-boundary diffusion, etc.). When the pressure in SPS increases up to several hundreds of MPa, powder agglomerates may break. The particle rearrangement at low temperature increases packing and reduces pore size, allowing homogeneous subsequent densification and limited grain growth. When temperature increases, additional densification mechanisms may occur, including plastic deformation or power-law creep (i.e., n typically takes more than 3). According to the above analysis [19], the rate-controlling mechanisms of the densification of tetragonal zirconia polycrystal (TZP) powders during SPS have been determined. When the applied macroscopic compaction stress is low and/or the temperature is low, a pure diffusion mechanism is responsible for the densification. At intermediate macroscopic compaction stresses and/or medium temperatures, a stress exponent of 2, associated with an apparent activation energy of 450 kJ/mol, has been determined; in this case, densification proceeds by grain-boundary sliding accommodated by diffusional mechanism controlled by the interface reaction. For high temperatures and/or high stresses, the stress exponent in a range of 3–5 suggested that densification proceeds by a dislocation-climb-controlled mechanism.

Historical Background of SPS

Historical background of SPS has been comprehensively described by Grasso et al. [20]. In short, direct origin of SPS machines in use today is "spark sintering" apparatus based on pulsed current, invented by Inoue in the early 1960s. However,

the commercialization did not come to a large success. After Inoue's patents expired in the late 1980s, Japanese companies (including Sumitomo Coal Mining Co., Ltd.) started the industrial production of "spark plasma sintering" machines. Since then, the practicality and reproducibility of SPS machines have been drastically improved, and the academic research as well as the industrial application has accordingly increased. Nowadays, more than ten companies from China, Korea, the USA, Germany, and Japan commercially produce ECAS/SPS apparatus.

Because SPS method features rapid and quick heating, homogeneous sintering of large components is a major issue from the beginning of the invention. In particular, in the material with a diameter of >100 mm, nonuniformity of stress and heating due to the thermal conductivity and particle rearrangement during SPS process poses significant problem for rapid and uniform sintering. However, recent technical progress and enlargement of SPS machines enable the manufacturing of large-size sintered Al_2O_3 bodies with a diameter of 300 mm [21]. Another recent SPS development is process automation. Five types of semi- or fully automated SPS manufacturing systems have been developed: multihead, batch, tunnel, rotary, and shuttle systems. Each type of apparatus is applied to specific condition of industrial application and product according to size and configuration, demanded characteristic production cycle time, production cost, and economics.

Materials of Transparent Ceramics

Efforts aimed at attaining transparency of polycrystalline ceramics focus on the parameters of density (or porosity) and grain size. As noted in section "Role of Microstructure on Optical Properties,". As described above pores and grain boundaries are light-scattering origins, but as has been shown, porosity plays a more determining role [7, 22]. Here several transparent oxide and non-oxide ceramics manufactured by SPS are briefly summarized, focusing on the critical factor(s) to determine transparency of polycrystalline ceramic body.

Al_2O_3

α-Al_2O_3, known as corundum, is a thermodynamically stable material with high strength, hardness, and corrosion resistance. Translucent or transparent polycrystalline Al_2O_3 has been used as light-transmitting component exposed at high temperatures and in corrosive environments, e.g., in high-pressure sodium lamps. Conventional translucent Al_2O_3 polycrystal is characterized by a very low porosity (<0.1%) and a relatively large grain size (>10 μm) [7]. However, several studies reported that sub-micron grain size is rather advantageous for improving the light transmittance of alumina (Fig. 4). For attaining transparency in fine-grained alumina ceramics, a full density or an extremely low porosity is a mandatory requirement. Since residual pores have a significant negative effect on light transmission, for transparent alumina, porosity should generally be reduced to less than 0.05%

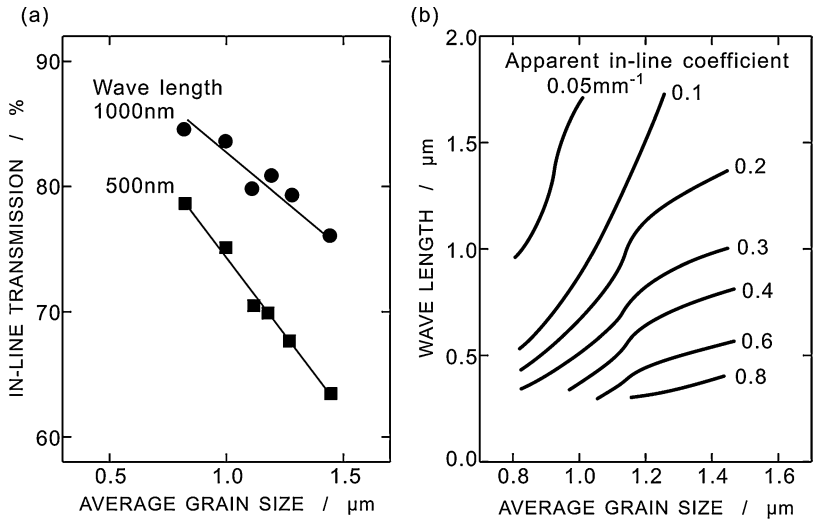

Fig. 4 (**a**) In-line transmission of fully densified Al_2O_3 polycrystals prepared by HIP as a function of the average grain size for wavelength of the incident light of 500 and 1000 nm. (**b**) Relationship between wavelength of the incident light and the average grain size for different apparent in-line coefficients in the fully densified Al_2O_3 polycrystals prepared by HIP [5]

[23]. Low porosity also allows good mechanical properties such as strength, wear resistance, and hardness. Traditional transparent Al_2O_3 ceramics were prepared by sintering in reducing atmosphere such as a mixture of nitrogen and hydrogen gases at temperatures of generally above 1700 °C [24, 25]. The high sintering temperature caused extensive grain growth, which in turn seriously degraded mechanical strength and hardness of the materials.

Transparent Al_2O_3 with fine-grain sizes can be also produced by using SPS technique [26–30]. For example, a fully densified (i.e., with the relative density of almost 100%) Al_2O_3 with a grain size of around 0.5 μm was obtained at 1200 °C by SPS [27]. During SPS of the alumina ceramics, the heating rate was usually set to a very high value (>100 °C/min), and the holding time at sintering temperature was set to be short (3–10 min); it has been believed that the short heating time at low temperatures can significantly suppress the grain growth during heating process, resulting in rapid densification by easy grain-boundary sliding and enhanced diffusion mass transport due to small powder particles under applied mechanical pressure.

However, in the last decade, it has been pointed out that low heating rate is rather effective to improve transparency of Al_2O_3 polycrystals prepared by SPS. Kim et al. found that grain size as well as porosity can be effectively reduced by retarding heating rate during SPS, leading to higher transparency of Al_2O_3 polycrystals [27], though rapid hearing rate is recognized as one of the advantages of SPS. They examined the microstructure and optical transparency in SPSed Al_2O_3 at a heating rate in the range of 2–100 °C/min. Figure 5 shows the grain size and porosity values of the sintered Al_2O_3 at the sintering temperature of 1150 °C for 20 min under the

compressive stress of 80 MPa. For the alumina sintered at 1150 °C for 20 min, the grain size was smaller at lower heating rates. The porosity was 0.59% at a heating rate of 100 °C/min and decreased to 0.02% at 10 °C/min and 0.002% at 2 °C/min. The heating-rate dependence of the porosity in Fig. 5 is quite similar to that of the grain size. Low heating rates resulted in small grain size and high density in the alumina polycrystals prepared by the SPS. Such an effect of the heating rate on the transparency has appeared not only in Al_2O_3 but also in $MgAl_2O_4$ and Y_2O_3, as described hereafter. Kim et al. assumed that an electric field and/or current may increase the concentration of vacancies in Al_2O_3 during SPS [29]. In fact, unusual rapid grain growth can be observed in Al_2O_3 sintered by rapid heating rate SPS [28]. A large DC current for heating could trigger the defect formation, resulting in small inter-/intragranular pores and reduced optical transparency in Al_2O_3 [29].

The theoretical in-line transmission was calculated by Apetz and Bruggen [7], on the basis of Rayleigh-Gans-Debye theory. When light scattering occurs only at grain boundaries (zero porosity), the theoretical in-line transmission T is represented as

$$T = (1 - R_s)\exp\left(-\frac{3\pi^2 G\Delta n^2 t}{2\lambda^2}\right) \tag{4}$$

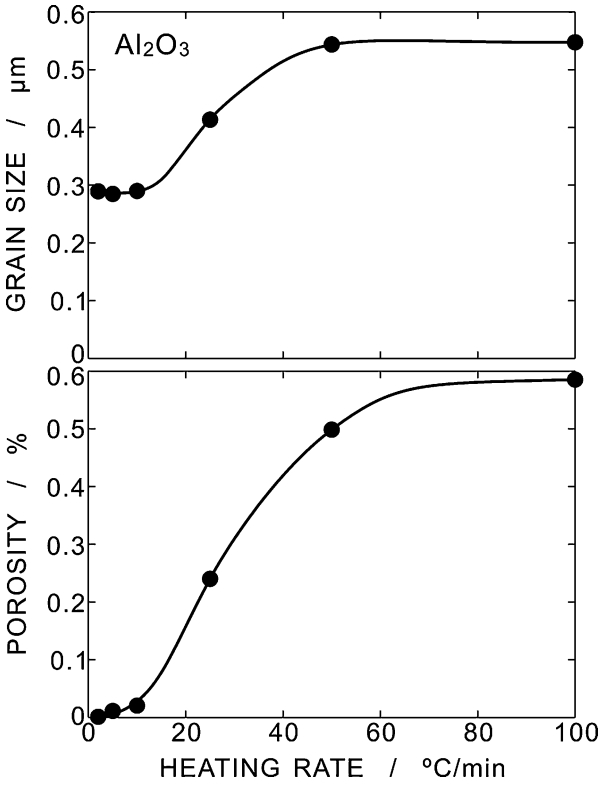

Fig. 5 The grain size and porosity values of the SPSed Al_2O_3 under different heating rates at the sintering temperature of 1150 °C for 20 min under the compressive stress of 80 MPa [28]

where R_s is the total surface reflection losses, G is the grain size, Δn is the refractive index difference (=0.0053), t is the sample thickness, and λ is the wavelength of the incident light. Calculating Eq. (4) with $d = 0.27$ μm, $t = 0.88$ mm, and $\lambda = 640$ nm, we obtain an in-line transmission of 68%. The in-line transmission in the Al_2O_3 bodies SPSed at different heating rates as a function of wavelength is shown in Fig. 6 [28]. Figure 6 also shows the theoretical prediction of Eq. (4) for zero porosity. The alumina changed gradually the appearance from opaque to transparent with decreasing heating rate. The transmission increases with the decreasing heating rate. The transmission-wavelength curves approach the value of heretical value (86%) with the increasing wavelength, whereas it decreases rapidly with the decreasing wavelength, particularly in the ultraviolet region ($\lambda < 400$ nm). Although the in-line transmission (46%) lower than the theoretical value is mainly due to the residual porosity, it is comparable to the transmission of 40–57% obtained by using HIP for the alumina doped with 0.03 wt% MgO [23]. As a result, during SPS of alumina, low heating rates resulted in fine-grain size, low porosity, and high transparency: for sintering at 1150 °C for 20 min, a grain size of 0.29 μm, a porosity of 0.002%, and an in-line transmission of 46% were obtained at a heating rate of 2 °C/min. The fine microstructure at low heating rates can be explained by using the assumption of low defect concentration and the low porosity (high density) by the accelerated grain-boundary diffusion owing to a large gain-boundary area. The authors concluded that slow heating also homogenized the powder during SPS, which should contribute to result in the fine microstructure and high density. The same tendency that lowers heating rate results in lower porosity and finer-grain size is also observed in Y_2O_3 and $MgAl_2O_4$, as depicted later.

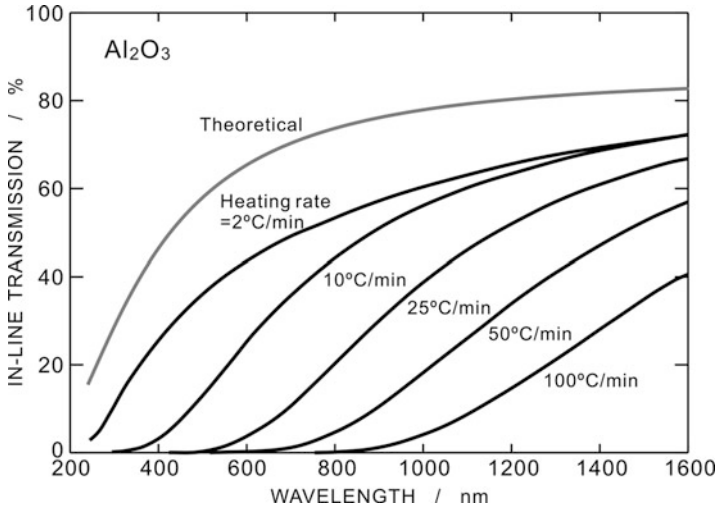

Fig. 6 The in-line transmission in the Al_2O_3 bodies SPSed at different heating rates as a function of wavelength [28]. The theoretical prediction of Eq. (4) for pore-free Al_2O_3 polycrystal is also depicted for comparison [23]

Recently, transparent, rare-earth-doped Al_2O_3 polycrystal for photoluminescent application has been successfully produced by SPS [31]. Tb^{3+} ions up to a concentration of 0.5 at% were incorporated into a dense alumina matrix by SPS at 1200 °C for 10–30 min, and a transmittance of about 75% at an incident light wavelength of 800 nm was obtained. The relative densities and average grain sizes in the SPSed materials were more than 99% and around 200–400 nm, respectively. These doped Al_2O_3 displayed photoluminescent peaks centered at 485 and 543 nm, which were characteristic of Tb^{3+} emission. This result shows great potential of SPS for manufacturing of alumina-based light-producing devices, such as high-powered lasers.

Y_2O_3

Y_2O_3 has excellent physical and chemical properties, such as a high melting point (2430 °C) and broad range of transparency (200–8000 nm). Y_2O_3 has a cubic crystal with group of Ia3. In addition, Y_2O_3 exhibits thermal conductivity of 13.6 W/mK at room temperature, thermal expansion coefficient of 8.7×10^{-6} 1/K, and refractive index of 1.93 (at 532 nm). These properties make Y_2O_3 a promising optical material. Y_2O_3 possesses a higher thermal conductivity and a lower thermal expansion coefficient than the widely used $Y_3Al_5O_{12}$ (YAG); the physical properties are critical for thermal management as laser powers continue to increase and generate heat during operation [32]. Furthermore, Y_2O_3 exhibits excellent resistance against fluorite plasma, which is generally used for etching of silicon wafer as semiconductor devices. The plasma-proof property of Y_2O_3 is in fact remarkably superior than Al_2O_3, sapphire, and YAG. Other potential applications of Y_2O_3 include infrared domes, nozzles, refractories, components of semiconductor devices, and efficient NIR-visible up-converters [33–35]. Due to its optical characteristics, Y_2O_3 has been mainly developed in transparent body for optical application.

Y_2O_3 is, however, difficult to sinter among oxide ceramics. It is also difficult to grow single crystals of Y_2O_3 to a large size due to its high melting point. Therefore, polycrystalline Y_2O_3 ceramics with a high optical transparency have been developed by pressureless sintering in a vacuum or hydrogen atmosphere at high temperature (typically >1600 °C) [36, 37], by HP sintering [38, 39] and by HIP process [40–42]. The first translucent Y_2O_3 ceramic was fabricated by pressureless sintering in hydrogen atmosphere at very high temperature of beyond 2000 °C, doped with 10 wt% of thorium oxide (ThO_2) particles as second crystalline phase [38].

HP and HIP are also effective techniques to produce transparent Y_2O_3. Hou et al. [43] fabricated transparent Y_2O_3 ceramics by using HP at 1800 °C for 20 h. Another example was reported by Podowitz et al. [44] by using HP at a maximum pressure of 40 MPa and a maximum temperature of 1580 °C. Optical transparency could be optimized through a stepwise application of pressure.

Several research groups have also attempted to produce transparent Y_2O_3 by SPS method. For instance, An et al. [45] reported the synthesis of transparent Y_2O_3

ceramics by using SPS at moderate temperature and pressure profiles. The samples sintered at 1300 °C and annealed at 1050 °C had a transmittance of 81.7% at wavelength of 2000 nm. Here, it is noteworthy that Y_2O_3 can be densified by low-temperature SPS at a sintering temperature of about or less than 1000 °C: translucent Y_2O_3 material can be synthesized from a commercial Y_2O_3 powder by the low-temperature SPS synthesis at 1050 °C for 1 h, exhibiting the in-line transmittance in a range of 6–46% in the wavelength range of 400–800 nm [17, 46]. In comparison with HP at the same sintering temperature and pressure, SPS was significantly effective to improve sinterability of Y_2O_3.

The effectiveness of SPS must result from the role of electric field/current and is probably related to the reduced state of Y_2O_3 under the application of pulsed field/current. As mentioned above, EELS analysis suggested that Y_2O_3 polycrystal consolidated by SPS exhibited reduced state in comparison to Y_2O_3 sintered in air and in vacuum. The pulsed DC field and/or current must induce excess anion vacancies and must accelerate diffusional mass transport and densification of Y_2O_3 materials. In fact, grain growth behavior in Y_2O_3 during SPS also indicated accelerated grain-boundary mobility under the pulsed DC field/current: according to the grain growth experiment in Y_2O_3 during isothermal SPS, grain-boundary mobility is highly enhanced by SPS in comparison with pressureless sintering of Y_2O_3. The grain-boundary mobility at 950 °C during SPS was comparable to the previously reported data for Y_2O_3 by pressureless annealing at around 1500 °C in air [17]. This result suggested that diffusion of yttrium cation in Y_2O_3 is highly accelerated by SPS process. It is possible that an electric field applied during SPS enhances some defect reactions that involve an electron emission. The SPS may activate the formation of oxygen vacancies and interstitial yttrium cations and consequently accelerate mass transport in Y_2O_3, leading to enhanced densification in low-temperature SPS.

Also, heating-rate dependence of the translucency of SPSed body has been investigated in Y_2O_3, and it has been found that low heating rate (2 °C/min) was preferable to produce high transmittance of the SPSed body, as well as SPSed Al_2O_3 described above. Furthermore, by employing high pressure, transparent Y_2O_3 body can be obtained even by low-temperature SPS. For example, transparent Y_2O_3 ceramics could be prepared at 1050 °C for 1 h with a heating rate of 10 °C/min under a uniaxial pressure of 300 MPa [47]. The obtained samples possessed nanometric grains (around 400 nm) and high density (>99.95%). Figure 7 shows in-line transmittance of Y_2O_3 densified by the low-temperature and high-pressure SPS under the uniaxial compressive stresses of 200 and 300 MPa, respectively. In-line transmittance of 68% at 700 nm and comparable performances of single-crystal yttria in the near-infrared wavelength region were attained in the Y_2O_3 body by the high-pressure SPS processing.

Recently, it has been reported that an addition of sintering aids can effectively improve the sinterability of Y_2O_3 during SPS process. Yoshida and co-workers investigate densification behavior and optical transparency of 1 mol% Zn^{2+}-doped Y_2O_3 consolidated by the SPS technique, by varying the most relevant process parameters, i.e., heating schedule, sintering temperature, holding time at the sintering temperature, and loading stress [48]. Transparent, Zn^{2+}-doped Y_2O_3

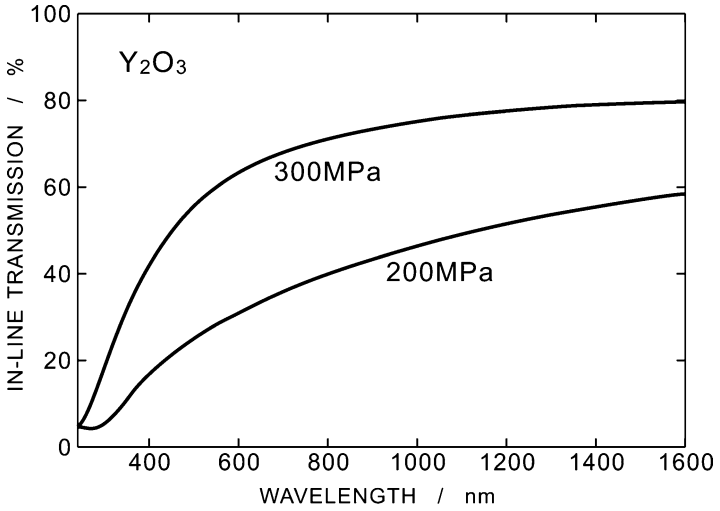

Fig. 7 The in-line transmittance of Y_2O_3 densified by the low-temperature and high-pressure SPS at 1050 °C for 1 h with a heating rate of 10 °C/min under a uniaxial pressure of 200 or 300 MPa [47]

polycrystals were successfully produced at the heating rate of 2 °C/min, sintering temperature of 890 °C, holding time of 30 min, and loading stress of 150 or 170 MPa. The grain size of the SPSed Zn-Y_2O_3 was about 200 nm, and the highest transmittance in the Zn^{2+}-Y_2O_3 bodies at a wavelength of longer than 600 nm was comparable to those in the undoped SPSed Y_2O_3 in the literature. The Zn^{2+}-doping effectively reduced the sintering temperature for fully densified Y_2O_3 by SPS; according to the literature, undoped Y_2O_3 was fully densified by SPS at 1050 °C and 200 MPa or 1300 °C and 100 MPa. High-resolution transmission electron microscopy analysis revealed that Zn^{2+} cations segregated in the vicinity of the grain boundaries. The grain-boundary segregation of Zn cations contributed to the reduction of the sintering temperature required for attainment of transparency in the Y_2O_3 by SPS.

ZrO_2

Zirconia ceramics have been used for various engineering applications since Garvie et al. [49] discovered phase transformation toughening in partially stabilized ZrO_2 (PSZ). The stable phases at high temperatures, i.e., tetragonal and cubic phases, can be stabilized by dopants that induce oxygen vacancies and/or are oversized with respect to Zr cations. Dopants of CaO, MgO, Y_2O_3, and CeO_2 are generally known as stabilizers of the tetragonal phase, and among them, Y_2O_3 is most extensively used as the stabilizer of zirconia ceramics in engineering applications. Y_2O_3-stabilized tetragonal ZrO_2 polycrystal (Y-TZP) with excellent mechanical properties has been the most extensively commercialized for use in optical fiber connectors

(ferrules), grinding media, precision parts, and dental applications. In addition, Y_2O_3-stabilized cubic ZrO_2 (c-YSZ) has been investigated as a candidate for a solid-electrolyte material in fuel cells because of its high oxygen anion conductivity. These properties strongly depend on the microstructures and phase stability in Y_2O_3-stabilized ZrO_2 (YSZ) [50]. For instance, excellent mechanical strength and toughness in Y-TZP are explained in terms of transformation toughening, in which crack propagation is inhibited by stress-induced, martensitic tetragonal-to-monoclinic (t-m) phase transformation; the t-m phase transformation yields the expansion of unit cell volume of approximately 4%.

Significant attention has been paid to the fabrication of optically transparent polycrystalline c-YSZ [51–53]. One of the motivations for the studies stood on the development of c-YSZ as a multifunctional ceramic with the combination of optical transparency (high refractive index of 2.2), excellent thermal properties, and high ionic conductivity. Since fully densified c-YSZ polycrystal is difficult to produce due to its rapid grain growth, polycrystalline c-YSZ is usually prepared at high temperatures using HIP [52–54] for high density and good transparency. For instance, transparent c-YSZ ceramics were made from cubic-stabilized ZrO_2 powder by sintering under vacuum at 1650 °C for 3 h, followed by HIP treatment at 1750 °C for 1 h at a pressure of 196 MPa [54]. Post-thermal annealing at 1000 °C was conducted to decolorize the as-sintered samples. The optical properties of these zirconia ceramics were comparable to those of their single-crystal counterparts. Owing to high sintering temperatures, however, the resultant materials typically have large grain sizes. The reduction of grain boundaries is preferable for optical transparency, but the coarsened grain size deteriorates the mechanical properties, which are also important requirements for optical applications.

In contrast with HIP and other common sintering methods, SPS enables fabrication of transparent c-YSZ ceramics with fine-grain sizes. For example, SPS was performed on a commercial 8 mol% Y_2O_3-stabilized cubic ZrO_2 powders at the sintering temperature of 1200 °C, heating rate of 200 °C/min, and pressure of 141 MPa, and transparent c-YSZ with the grain size of 55 nm was successfully obtained [55]. The SPSed samples became increasingly deep red in color with the increasing holding time. Darkening of the nanostructured c-YSZ was probably attributed to excess oxygen anion vacancies caused by the highly reducing environment of hot graphite.

Another example is the use of high-pressure SPS for production of transparent c-ZrO_2 from a commercial raw powder [56, 57]. A nanosized cubic ZrO_2-8 mol% Y_2O_3 powder was consolidated by using SPS at 1000 °C under a pressure of 600 MPa, resulting in the final grain size of around 50 nm and the transmittance in the near-infrared region (1-mm-thick samples) of higher than 60% [56]. Taking into account the reflective losses of the end surfaces, the maximum allowable transmittance for the SPSed c-YSZ was between 70% and 80% of the theoretical value. In the c-YSZ specimens, the residual porosity was about 0.01, and the pore size was less than 20 nm, which was too small to produce significant scattering. It is suggested that the observed light absorption in the SPSed c-YSZ was related to the presence of large amounts of color centers, generated by the reducing environment in the SPS

processing. In another case, commercial 8 mol% Y_2O_3-ZrO_2 powders were consolidated by employing SPS with the optimum conditions of the sintering temperature, pressure, heating rate, and soaking time of 1100 °C, 400 MPa, 10 °C/min, and 10 min, respectively [57]. The as-sintered zirconia exhibits a yellowish-brown appearance, which is a typical phenomenon in oxide ceramics produced by SPS. This discoloration is related to the formation of oxygen anion vacancies. In fact, annealing in oxidizing environment at 700 °C for 100 h can reduce oxygen vacancies through diffusing oxygen back into c-YSZ. Typical in-line transmittance spectrum of the post-SPS annealed c-YSZ is shown in Fig. 8. TEM observation revealed that the SPSed c-ZrO_2 exhibited uniform, very fine, and equiaxed microstructure with the average grain size of 30 nm.

In contrast to c-YSZ, it is difficult to improve transparency in tetragonal ZrO_2 ceramics even by SPS techniques. SPS processing is actually effective to suppress grain growth during sintering, so that fully densified TZP ceramics with grain sizes of 50–55 nm have been obtained by using SPS [55]. However, dense tetragonal ZrO_2 ceramics were less transparent than fully densified c-YSZ, though the TZP and c-YSZ materials have the same density and grain size. For instance, translucent tetragonal ZrO_2 doped with 3 mol% Y_2O_3 ceramics was produced by SPS processing from nanosized raw powders [56]. The typical SPS conditions were at 1000 °C for 5 min under a pressure of 800 MPa. The tetragonal ZrO_2 ceramics had an average grain size of about 50 nm. The transmittance with 1 mm thickness was >50% in the near-infrared region but was less than 20% in visible light region for the tetragonal ZrO_2 ceramics. The samples had a yellowish-brown color, which

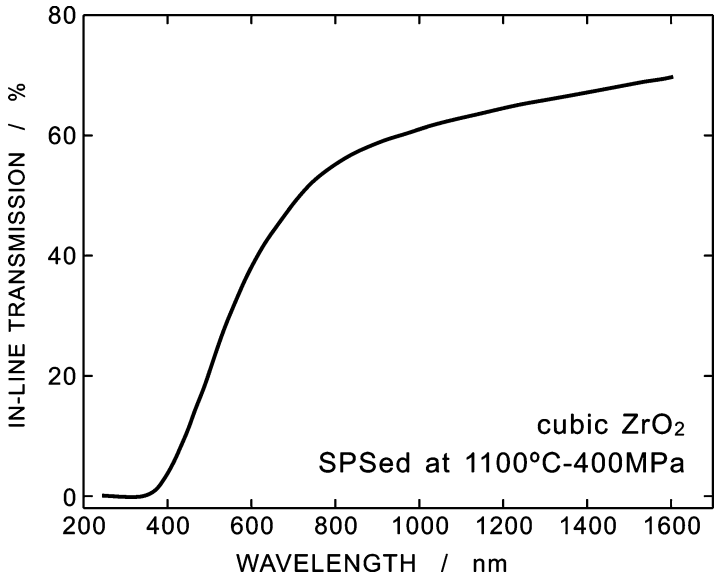

Fig. 8 Typical in-line transmittance spectrum of 8 mol% Y_2O_3-stabilized cubic ZrO_2 SPS at 1100 °C and 400 MPa followed by annealing in oxidizing environment at 700 °C [57]

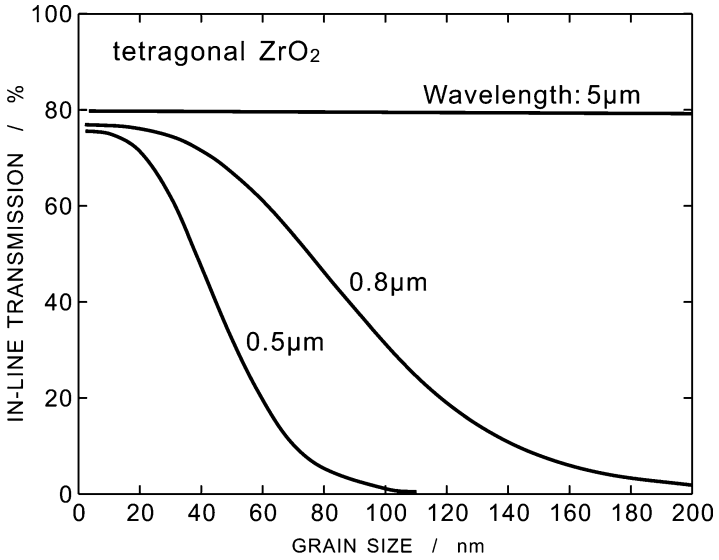

Fig. 9 Predicted in-line transmission of fully dense sintered tetragonal ZrO_2 (thickness 1 mm) without absorption calculated for a grain size <200 nm using Mie theory for mean birefringence in range 0.03–0.04 for visible light and 0.035 for IR wavelength [58]

was attributed to the presence of color centers. It was confirmed that optical birefringence was the main factor that limited the transparency of pore-free, tetragonal ZrO_2 ceramics. Klimke and co-worker predicted the conditions to obtain transparent tetragonal ZrO_2 ceramics by comparing the experimental data for sintered nanopowder with scattering calculations [58]. Figure 9 shows predicted in-line transmission data of fully dense sintered tetragonal ZrO_2 (thickness 1 mm) without absorption calculated for a grain size <200 nm using Mie theory for mean birefringence in range 0.03–0.04 for visible light and 0.035 for IR wavelength [58]. According to their calculation, in-line transmission of about 50% at visible light and 1 mm thickness is expected at a mean grain size <40 nm. In order to obtain a better quality with transmission of 70%, for instance, grain size of less than 20 nm is required according to the calculation. In addition, the influence of grain size becomes insensitive in the IR region; at an IR wavelength of 5 μm, there should not be any scattering caused by birefringence for grain sizes <200 nm.

MgO

MgO shows a high melting point of 2850 °C and low density of 3.58 g cm^{-3}, though vapor pressure of MgO is relatively high in comparison to other oxides such as

Al_2O_3 and ZrO_2. MgO has an isotropic cubic crystal structure, which is desirable for attainment of transparency. Polycrystalline infrared-transparent MgO is a potential substitute for sapphire IR windows and protectors for sensors.

Dense MgO ceramics have been produced by the traditional sintering method, such as pressureless sintering and vacuum sintering [59–61]. Chen et al. fabricated translucent MgO ceramics by sintering at 1400 °C for 2 h under ambient atmosphere from the MgO powders synthesized via a wet precipitation process, and the average grain size of the ceramics was about 6 μm [60]. Suzuki et al. reported that transparent MgO ceramics with an average grain size of about 10 μm were prepared by sintering the powders at 1600 °C for 3 h in an oxygen atmosphere with the existence of chloride ion [61]. The conventional techniques for the fabrication of dense MgO ceramics require high sintering temperature (typically >1400 °C), which leads to coarsened grains in sintered body. The preparation of MgO ceramics using HP or HIP method was also previously studied [62–65]. Itatani et al. reported that translucent MgO ceramics with a relative density of 99.7% and grain size of about 0.8 μm was obtained by HP at a temperature of 1100 °C for 30 min [65]. In addition, HIPing of pressureless sintered MgO body at 1500–1600 °C produced transparent MgO ceramics with the average grain size in a range of 100–200 μm [65]. Addition of LiF a is common technique to prepare transparent MgO by vacuum HP of MgO [66, 67]. The addition of LiF as sintering aid could reduce the sintering temperature of MgO transparent ceramics [68, 69]. It has been acknowledged that densification of MgO with LiF was enhanced due to the formation of a liquid phase [70].

The SPS process was also used for fast densification of the MgO ceramics, yielding a high density and fine-grain sizes. For example, densification of nanocrystalline MgO powders by SPS was examined at SPS temperature between 700 °C and 825 °C under applied pressures of 100 and 150 MPa [71]. As a result, fully densified transparent nanocrystalline MgO with a 52 nm average grain size was fabricated by the SPS at 800 °C and 150 MPa for 5 min. In-line transmissions of 40% and 60% were attained compared to MgO single crystal, for the yellow and red wavelengths, respectively. Tran et al. reported a fully dense Ca-doped MgO ceramics with a transmittance of about 90% in the IR range and a final grain size of 25–70 nm, prepared by SPS at 650–800 °C under a uniaxial pressure of 300–500 MPa [72]. Liu et al. reported that undoped MgO ceramics with a relative density of 99.1% and an average grain size of 50 nm were obtained at 1347 °C with the utilization of an ultrahigh heating rate (>1700 °C/min) and high pressure (up to 170 MPa) by the combustion reaction plus quick pressing method [73]. In another case, Jiang and co-workers investigated the effect of LiF addition on SPS of MgO [74]. In their experiments, transparent MgO ceramics doped with 1 wt% LiF were successfully obtained by SPS at 900 °C with the heating rate of 100 °C/min under the pressure of 30 MPa, and the corresponding grain size was about 0.7 μm. The transmittance of the transparent MgO ceramics (1.5 mm thick) was above 85% in the range of 3–5 μm. The recent studies have proved that SPS processing is beneficial in the production of transparent and fine-grained MgO ceramics.

$MgAl_2O_4$

Magnesium aluminate ($MgAl_2O_4$) spinel is a synthetic material with cubic crystal structure and excellent thermal, mechanical, and optical properties [75]. High optical transmission for visible and IR wavelength range in $MgAl_2O_4$, in particular, is attractive for various optical applications. These properties made $MgAl_2O_4$ an indispensable material for optically transparent windows, domes, and armors and for certain refractory applications. The spinel does not exhibit birefringent scattering at its grain boundaries owing to the symmetric cubic crystal structure and, hence, can exhibit an excellent transparency even in the polycrystals. For engineering applications, because the shape forming by powder processes is an economical route rather than the machining from single crystals, the development of a simple powder processing method is desirable.

However, spinel powder is difficult to sinter, and the fabrication of full-dense and transparent spinel polycrystals involves high costs through conventional routes such as pressureless sintering. The volume expansion (about 8%) associated with $MgAl_2O_4$ phase formation from alumina and magnesia does not allow obtaining dense $MgAl_2O_4$ bodies in a single-stage reaction sintering process [75]. Thus, in most of the earlier studies, dense polycrystalline spinel has been obtained through high-temperature conventional sintering (typically >1500 °C) [76, 77], HP [78–80], and HIP [81–84]. Sintering aids such as LiF [85], CaO [86], and B_2O_3 [87] have also been used for consolidation of spinel powder. Densification using sintering aids and/or high sintering temperatures, however, often causes grain coarsening, and this may degrade the mechanical properties. In the viewpoint of engineering application, fine-grained materials are desirable due to their high mechanical strength. SPS has been therefore employed [88, 89] for production of transparent $MgAl_2O_4$ bodies.

In SPS processing of $MgAl_2O_4$ spinel ceramics, significant heating-rate dependence of the transparency of sintered bodies were pointed out, as well as in the case of Al_2O_3. For instance, according to the report by Morita et al. [89], high transmission was attained by reducing residual porosity and pore size, which were achieved by the application of low-heating rate. At high heating rates, many closed pores were formed due to the high densification rate during the heating process and remained as large pores at the grain junctions. The heating-rate dependence on in-line transmission in the SPSed $MgAl_2O_4$ spinel ceramics sintered at 1300 °C for 20 min under the pressure of 80 MPa is shown in Figure 10. The plots of transmission clearly show that the heating rate influences the transmission, particularly in the visible-wavelength range. For sintering at 1300 °C, the transparency increases with the decreasing heating rate.

It is generally accepted that mechanical properties such as flexure strength and hardness of polycrystalline materials are gained by the reduction of their grain sizes. The improved mechanical strength is often depicted by Hall-Petch law; the strength of material is proportional to the inverse of square root of grain size. The strength-grain size relationship has been reported not only in metallic but also ceramic materials so far. Figure 11 shows Vickers hardness as function of square root of grain size for SPSed $MgAl_2O_4$ spinel materials [90]. The SPSed $MgAl_2O_4$ spinel

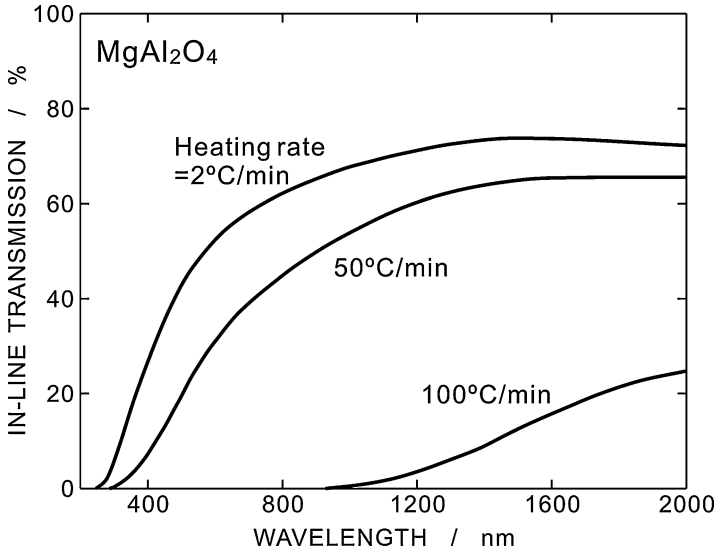

Fig. 10 Heating-rate-dependent in-line transmission in $MgAl_2O_4$ spinel plotted as a function of wavelength [89]

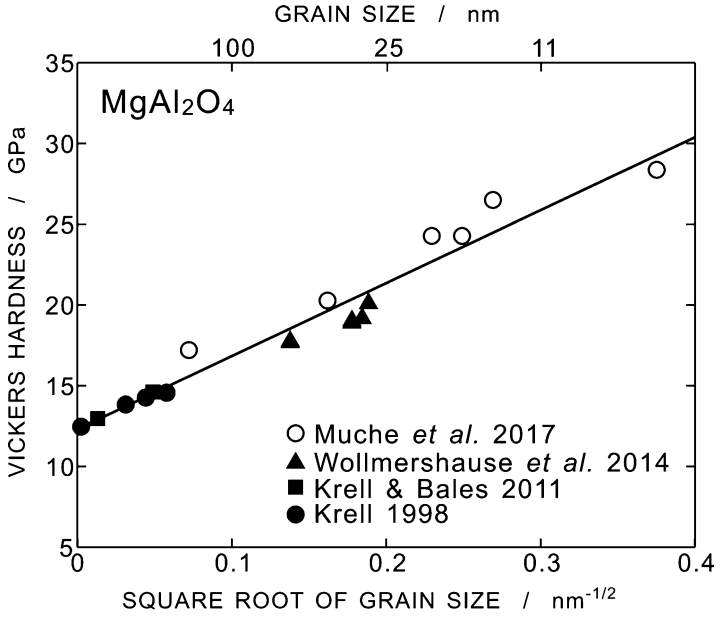

Fig. 11 Vickers hardness as function of square root of grain size for the SPSed $MgAl_2O_4$ spinel ceramics [90]. Literature data [88–90] for spinel ceramics at different grain sizes are plotted as a comparison. The straight line represents the trend line for linear response of Hall-Petch relationship in terms of inverse of the square root of the grain size

materials were prepared at 720–870 °C for 4–5 min under 1.4–2.0 GPa. Literature data for $MgAl_2O_4$ spinel at different grains sizes are plotted as a comparison. Nanocrystalline $MgAl_2O_4$ spinel has limited reports with grain sizes lower than 100 nm, and no studies have been reported in the literature for grain sizes below 20 nm. The straight line represents the trend line for linear response of Hall-Petch relationship in terms of the inverse of square root of grain size. As a result, no correlation of Hall-Petch relation is observed down to the smallest tested size. As shown in Fig. 11, the refinement of grain size is beneficial for the improvement of mechanical properties as well as transparency of optical ceramic materials.

It is noteworthy that the origin of discoloration observed in fully densified, SPSed $MgAl_2O_4$ has been revealed by spectroscopic techniques. Discoloration after SPS synthesis is often seen in various ceramics, and the discoloration has been regarded as a major source of limited light transmission. Recently, Morita et al. extensively investigated the origin of the discoloration in SPSed $MgAl_2O_4$ spinel by Raman spectroscopy, Fourier transform infrared (FT-IR) spectroscopy, and transmission electron microscopy [91]. According to their analysis, the discoloration is explained by the combination of carbon contamination and lattice defects (color centers), which are introduced in the spinel matrix depending on the SPS conditions. For low heating rates of 10 °C/min, trace carbonate CO_3 preexisting in the starting raw powder remained as glassy carbon, irrespective of the sintering temperature. For a high heating rate of 50 °C/min, additional carbon contamination occurred by evaporating the carbon phases from the carbon papers and graphite dies during the heating process and showed a tendency to be enhanced by the increasing heating rate. The color center (F^+-center) may be generated by the formation of oxygen vacancies. Since the rate of sintering, namely, the deformation rate, increased with the increasing heating rate, the concentration of the dislocation-related color centers may increase with the heating rate, but may decrease with the increasing sintering temperature due to the reduction of the oxygen anion vacancies.

For the spinel, the contamination was sensitive to the SPS conditions, such as the heating rate and loading schedules, but less sensitive to the sintering temperature. This suggested that the carbon contamination was caused by evaporation of CO gas from the carbon paper/dies. At the high heating rates, the carbon evaporation is enhanced due to the rapid heating, and then the evaporated CO gases are encapsulated into the closed pores during the heating process and remain in the matrix. The carbon contamination can be suppressed by a high-temperature loading even at the high heating rate [92].

$Y_3Al_5O_{12}$ (YAG)

Yttrium aluminum garnet $Y_3Al_5O_{12}$ (YAG) is one of the three stable phases in Y_2O_3-Al_2O_3 system. YAG has a cubic crystal structure [93] and therefore shows isotropic optical properties. Owing to its high thermal stability and homogenous optical properties, transparent YAG ceramics are applied to an excellent host material for fluorescence application and high-power solid-state lasers [94]. Nd and Er cations

are typical dopants of YAG for laser application. Ce-doped YAG (Ce:YAG) is used as phosphor in cathode ray tubes and white light-emitting diodes and as scintillator.

It is well-known that excellent transparent, Nd-doped YAG ceramics can be produced by solid-state reaction sintering in vacuum at 1750 °C for 10 h with the addition of tetraethyl orthosilicate (TEOS) [94]. One of the procedures that has been put forward for the manufacture of a polycrystalline laser material is a multistage process of high-temperature vacuum sintering followed by HIP in the 1450–1550 °C range for 5 h under 200 MPa argon, yielding high optical quality transparent YAG with a grain size of 1–2 μm [95].

Transparent, undoped YAG ceramics have been fabricated by various technologies, including vacuum sintering, HP, and HIP. Zych and Brecher [96] derived YAG transparent ceramics from the mixture of Y_2O_3 and Al_2O_3 by using HP at 1750 °C for 4 h under a pressure of about 300 atm. SPS was also applied to fabricate transparent YAG ceramics [97–99]. One example of SPS conditions for manufacturing transparent YAG was the sintering temperature of 1400 °C and duration time of 3 min using nanocrystalline YAG powders as starting material. In this case, fully dense and transparent polycrystalline cubic YAG ceramics with micrometer-grain sizes were obtained. In another case, transparent YAG was produced by SPS from nanocrystalline YAG powder dispersed by ultrasonication: heating rate, sintering temperature, duration time, and applied stress employed were 8 °C/min, 1325 °C, 15 min, and 74 MPa, respectively. As a result, fine-grained (330 nm), transparent YAG ceramics was obtained with the transmittance of 66% at the wavelength of 600 nm [99]. Moreover, transparent YAG doped with 0.25 wt% of LiF was also produced by SPS at 1300 °C for 2 h under a pressure of 80 MPa [98]. The addition of LiF promoted transparency of YAG body but increased grain growth during SPS.

Hydroxyapatite

Hydroxyapatite ($Ca_{10}(PO_4)_6(OH)_2$: HA) is a major component of human bone. A range of HA-based biomaterials have been developed for biomedical applications [100, 101]. Several studies have shown that transparent HA ceramics enable direct observations of living cells on HA substrates to determine the interactions between HA and cell/tissue [102–104]. Transparent HA materials have been fabricated using a range of sintering methods, such as HIP [105–107], microwave sintering [108], and SPS [109, 110]. For instance, a transparent HA material, which exhibited an in-line transmittance of 30–73% over the wavelength range of 400–700 nm with a very fine-grain size of less than 200 nm, was fabricated by SPS at 1000 °C from nanoparticle raw powders [110].

It should be noted that the transparent, fine-grained hydroxyapatite prepared by SPS exhibited superplastic deformation. Superplasticity is a characteristic of polycrystalline material, which exhibits large elongation to failure in tensile manner. High-strength, structural ceramics is in general very brittle, with limited plastic deformability. But if the grain size is reduced to typically less than 1 μm, then even structural ceramics can show superplastic deformation. SPSed hydroxyapatite

is the same situation such that fully densified and nanostructured body was obtained owing to the SPS process. The superplasticity can be applicable for near-net shape forming and joining of structural materials, and hence a number of studies were performed to improve superplasticity, i.e., increasing tensile ductility, reducing superplastic temperature, and accelerating deformation rate, in structural ceramics such as TZP. The superplastic flow behavior of transparent, nanocrystalline HA specimen prepared by SPS at 1000 °C was examined at temperatures ranging from 950 °C to 1050 °C [111], and the HA specimens exhibited superplasticity under the test conditions examined. An elongation of 270% was obtained even at 950 °C and an initial strain rate of 1.0×10^{-3} s^{-1}. A maximum elongation of 486% (nominal strain) was achieved at 1000 °C and an initial strain rate of 1.0×10^{-4} s^{-1}. The tensile ductility in this material was located in the upper portion of the existing data in HA materials. The post-deformation microstructure of HA indicates that grain-boundary sliding was the predominant mechanism of superplastic flow. The improvement in superplasticity in transparent, nanocrystalline HA arose essentially from the very fine-grain size and fully densified, pore-free microstructure.

AlON

Aluminum oxynitride (AlON) has a cubic spinel structure with chemical formula of $Al_{(64+x)/3}O_{32-x}N_x$ ($0 \leq x \leq 8$) and is a stable solid solution within the Al_2O_3-AlN system. AlON shows optical transparency over the region from near-ultraviolet to visible and near-IR wavelength. The cubic structure of AlON exhibits isotropic optical properties. Furthermore, AlON possesses excellent mechanical properties; strength and hardness of AlON are known to be superior to conventional sapphire and $MgAl_2O_4$ spinel. With the combination of good optical and mechanical properties, AlON can be used in defense and commercial applications, such as military aircraft missile domes, transparent armors, IR windows, hyper-hemispherical domes, laser windows, military aircraft lenses, semiconductor processing applications, and scanner windows [112]. Unfortunately, AlON ceramic is very difficult to sinter because of its high phase formation temperature and low sintering activity or diffusion coefficient. Conventional synthesis of AlON ceramics usually needs very high sintering temperature (typically higher than 1850 °C) for a long period (>20 h) [113, 114]. In addition, the high sintering temperature and long sintering time can easily lead to excessive grain growth and coarse microstructure, which in turn seriously lowers the optical properties and mechanical strength of the materials.

Transparent AlON bodies have been made by various sintering techniques, such as HP [115], HIP [116, 117], microwave sintering [112], or SPS [118–120]. In SPS, for instance, compacted powder of AlON doped with 0.5 wt% Y_2O_3 was first heated to a temperature in a range of 1350–1500 °C at a heating rate of 100 °C/min; then, after holding for 10 min, the heating system was shut down, and the furnace was cooled down to room temperature [120]. The axial pressure was maintained at a level of 40 MPa during the entire sintering process. As a result, the obtained samples sintered at 1350 °C and 1400 °C exhibited high infrared transparency. Figure 12

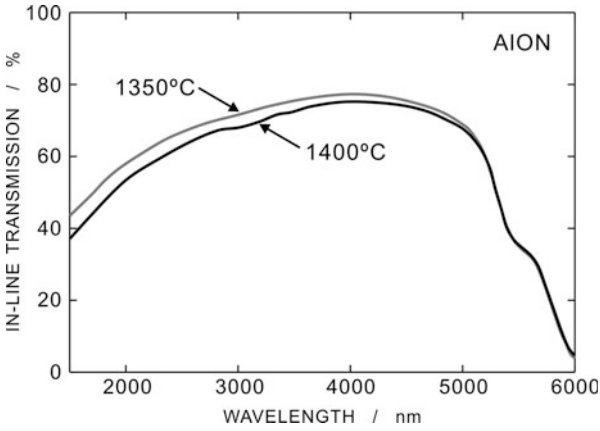

Fig. 12 The transmittance of AlON ceramics (1.2 mm in thickness) fabricated at 1350 °C and 1400 °C [120]

shows the transmittance of the materials (1.2 mm in thickness) fabricated at 1350 °C and 1400 °C. The maximum infrared transmittance of SPS-processed samples at 1350 °C for 10 min is 77.3% at around 3900 nm. At the same time, the sintered samples have high hardness of 18 GPa. The SPSed materials showed bimodal microstructure comprising the peak grain sizes of 5–10 and 2–3 μm. The high density and small grain size contribute also to the high hardness of the processed transparent ceramics. Similar to other ceramic materials, SPS technique is effective to produce transparent AlON ceramic with excellent mechanical properties.

AlN

Aluminum nitride (AlN) ceramics has attracted greater attentions recently due to their high intrinsic thermal conductivity (320 W/mK), low dielectric constant, thermal expansion coefficient matching with silicon (4.8×10^{-6} 1/K), and good electrical insulation properties. AlN ceramics with a wide band gap of 6.3 eV show great potential as transparent optical and window materials [121–123].

However, AlN is difficult to sinter, because of its strong covalency with wurtzite crystal structure. AlN ceramics with high density have been fabricated by using additives as sintering aids, such as alkaline earth oxides, rare-earth oxides, or mixtures of oxides, fluorides, and carbides. Because of their low sinterability and high impurity levels, the fabrication of transparent AlN bodies has proven to be more difficult than fabrication of oxide ceramics. For example, Kuramoto et al. [122–124] fabricated transparent AlN polycrystals by HP process at 1850–2000 °C for 3–10 h in nitrogen flow with CaO, $3CaO\text{-}Al_2O_3$ as an additive or even without additive.

Additives have been widely used for sintering high-quality ceramics. For instance, commercial AlN nanopowders doped with 3 wt% amount of CaF_2, Y_3O_2, or MgF_2 were consolidated by HP process at 1800 °C for 3 h under compressive pressure of 30 MPa at a rate of 5 °C/min under a nitrogen atmosphere [125]. As a result, the AlN ceramics prepared from nanopowders exhibited high

transparency. The maximum in-line transmittance is 53.2% at 1910 cm^{-1} for the CaF_2-doped AlN ceramics, 28.1% at 1817 cm^{-1} for the Y_2O_3-doped AlN ceramics, and 12.7% at 1820 cm^{-1} for the MgF_2-doped ceramics, respectively. Among these sintering aids, yttrium oxide is one of the most commonly used oxide additives, because it can react with the low-activity alumina layer on the surface of nitride particles and form liquid-phase yttrium aluminates to promote densification [126–128]. However, the yttrium aluminates formed and distributed along the AlN grain boundaries seriously reduce their transparency. In addition, non-oxide additives including fluorides are also adopted, which promote the densification process by liquid-phase sintering along with clean grain boundaries by evaporation of the secondary phase [129, 130].

SPS has also been used as an effective densification method of AlN ceramics. For example, dense AlN ceramics were prepared by SPS at a sintering temperature of 1700 °C and a heating rate of 100 °C/min under 40 MPa in a nitrogen atmosphere by using 2 wt% of Y_2O_3, Sm_2O_3, or Dy_2O_3 as sintering additives [131]. Fine-grained AlN ceramic with grain size of less than 1 μm was synthesized from AlN nanopowder with 1 wt% of $Ca_3Al_2O_6$ by SPS at 1450 °C for 5 min under 50 MPa of compressive stress [132]. Highly transparent, undoped AlN ceramic was successfully fabricated by SPS technique at the sintering temperature of 1800 °C, compressive pressure of 25 MPa, with different heating rates of 100–550 °C/min, and with sintering duration ranging from 4 to 20 min [133]. In another case, undoped AlN and SrF_2-doped AlN ceramics were consolidated by SPS, and the doped AlN exhibited translucency at the wavelength of longer than 500 nm [134]. SPS technique is an effective method for fabrication of transparent AlN ceramics, as it shortens sintering time and lowers sintering temperature.

Zinc Sulfide (ZnS)

Zinc sulfide (ZnS) has been widely used in many applications, such as optical elements, phosphors, sensors, and photocatalysts. In the wavelength range 8–14 μm, ZnS is a desirable candidate for the IR-transparent ceramics used in military and commercial applications [135, 136]. High-purity ZnS can be used for infrared window and missile dome in defense applications. Dense, IR-transparent ZnS ceramics have been produced by HP [137, 138], chemical vapor deposition (CVD), and CVD followed by HIP [139]. For instance, infrared-transparent ZnS ceramics with transmittance of 77% at wavelengths of 6.74 and 9.29 μm were manufactured by HP at 1000 °C for 3 h under a uniaxial pressure of 50 MPa at a heating rate of 5 °C/min under a vacuum of 10^{-5} mbar [136].

However, high-temperature sintering often causes a decrease in mechanical strength and hardness due to grain growth [140]. In addition, the phase transformation of ZnS ceramics at the relatively low temperature caused deterioration of transparency; the existence of hexagonal phase may pose birefringence that significantly decreases the optical transparency of ZnS ceramics. One of the effective approaches to avoid the drawback is to fabricate ZnS material at lower temperature.

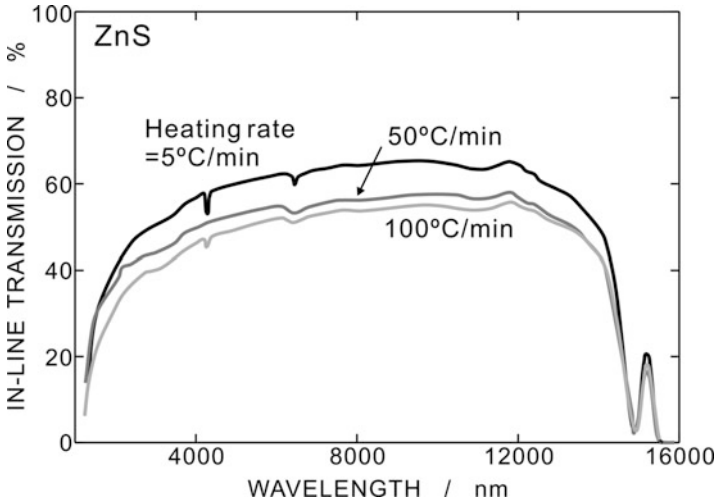

Fig. 13 Transmission of SPSed ZnS bodies with different heating rates from 5 °C/min to 100 °C/min [135]. The thickness of the specimens was 1.5 mm

Therefore, SPS synthesis has been applied to consolidate fully densified ZnS ceramics. Chlique et al. [141] demonstrated ZnS ceramics by SPS sintering with thickness of 0.55 mm, and the transmittance was up to 50% in the range of 8–14 μm.

In another case, the effect of heating rate in SPS processing was extensively investigated to obtain transparent ZnS [135]. The SPS synthesis conditions employed were heating rate in a range of 5–100 °C/min, sintering temperature of 840 °C, sintering time of 5 min, and compressive stress of 80 MPa. As a result, ZnS ceramics with good optical transparency were successfully fabricated at the relatively low SPS sintering temperature with the heating rate of 5 °C/min. The highest in-line transmittance of the SPSed ZnS ceramic body was up to 40% in the wavelength range of 2.0–3.0 μm and 60% in the infrared wavelength range of 5.0–12 μm, as shown in Fig. 13. The content of hexagonal phase of ZnS decreased with the decreasing heating rate.

New Technologies of ECAS/SPS

SPS has five major operating parameters, i.e., field/current waveform, sintering temperature, sintering time, heating rate, and compressive pressure. In order to efficiently manufacture transparent ceramics by SPS, it is important to optimize these parameters, as described above. Recently, more complex schedules of heating and pressurizing as well as energizing electric power have been adopted. Various attempts have also been made to improve the transparency of specimens by changing the material of the die and punches; thermal and electric conductivities directly influence sintering behavior of materials. In addition, new

technologies of ECAS have also been proposed one after another, and several techniques capable of extremely high sintering densification rate have been developed, while transparent body has not yet been produced by such quick and rapid ECAS techniques. Among new ECAS technologies, flash sintering is particularly attracting attention from academic and industrial circles.

Multistep SPS

In conventional sintering, it is well-known that multistep sintering, in which furnace temperature is raised not at uniform heating rate but at more than two steps of heating schedule, is effective for densification and grain size refinement of some ceramics. Most remarkable example was two-step sintering, in which sample was heated to a higher temperature then immediately cooled to a lower temperature for isothermal sintering with a dwelling time of more than several hours [142]; fine-grained and fully densified oxide ceramics, such as Y_2O_3 and $BaTiO_3$, were successfully manufactured. SPS has also attempted to introduce multiple steps into the temperature elevation and pressurization process. Several successful fabrication approaches have been presented.

A two-step pressure method, which enabled a significant improvement in in-line transmittance of high heating rate SPSed alumina was reported by Grasso and co-workers [143]. Commercially available alumina powder could be consolidated at 1150 °C by using SPS at a heating rate of 100 °C/min. The effects of pressure application mode were examined with respect to microstructure, porosity, and transparency. The pressure was applied in two ways. In the first case, a constant pressure of 80 MPa was applied for the entire duration of the sintering process (hereinafter, constant pressure). In the second case, an initial pressure of 35 MPa was applied; subsequently the pressure was increased in 3 min after the beginning of dwelling time (hereinafter, two steps pressure). The application of two-step pressure was found to be very effective to obtain homogeneously densified translucent alumina samples at high heating rate.

Transparent, undoped, and Nd-doped $MgAl_2O_4$ ceramics were produced by SPS with a two-step schedule: fast heating (100 °C/min) with a first dwell of 3 min at 1100 °C without high pressure and then heating at 20 °C/min to 1300 °C for 15 min under progressive uniaxial loading at 130 MPa [144]. Two-step sintering is also effective to densify 8 mol% Y_2O_3-stabilized cubic ZrO_2 by low-temperature SPS at 1050 °C [145]. In another case, nanocrystalline TiCN ceramics were fabricated by SPS in a multiple-stage regime with sequential increase of pressure from 50 to 70 MPa and simultaneous decrease of heating rate from 100 °C/min to 20 °C/min; the application of multiple-stage regime was beneficial for reduction of grain size and increment of mechanical properties, in comparison to traditional single-stage SPS regime [146]. When using intermediate pressures and standard graphite tools, a two-step pressure schedule might be advantageous to homogenize the microstructure [147].

Water-Assisted SPS Process

In recent years, the role of water in sintering densification has attracted attention; enhanced or suppressed sintering rates of various oxide ceramics in the presence of water vapor have been observed. In ECAS, it has been experimentally shown that the presence of water (or water vapor) contributes to the improvement of densification in several ceramics [148–150]. Due to the presence of water, the sintering temperature is drastically reduced. It is therefore expected to manufacture ceramics having microstructures and material properties unprecedented so far.

It has been recently reported that nanocrystalline zinc oxide (ZnO) was processed by SPS to a density above 95% at only 400 °C, which is significantly lower than common sintering temperature even in SPS techniques [149]. Reasons for this unexpected behavior are enhanced particle rearrangement and higher diffusivity, due to the presence of water adsorbed on the surface. Figure 14 shows the densification curves for humidified (1.6 wt %) and dried raw ZnO powder sintered using SPS at a high heating rate of 100 °C/min and maximum temperatures of 400 °C and 800 °C, respectively. The initial green density and the densification behavior of nanocrystalline ZnO are both enhanced by the presence of water in comparison to dry condition. The densification rate is strongly increased by humidification resulting into 99% of the theoretical density for humidified ZnO at 400 °C, whereas dried powder shows a residual porosity of 38% at the same temperature. In addition, full densification is achieved after an isothermal sintering time of only 10 min. Typically the full densification of nanocrystalline zinc oxide by means of HP or SPS requires much longer isothermal durations of more than 1 h and a sintering temperature of at least 800 °C.

According to the authors' analysis, the densification of nanocrystalline ZnO increased with the increasing fraction of surface bound water. Apparent activation energy for sintering densification decreased with the increasing water fraction, indicating a modification in sintering mechanism. The formation of oxygen-hydrogen-related defect complexes was suggested in Kelvin probe force microscopy analysis, and such an interface interaction of surface bound water with the grain

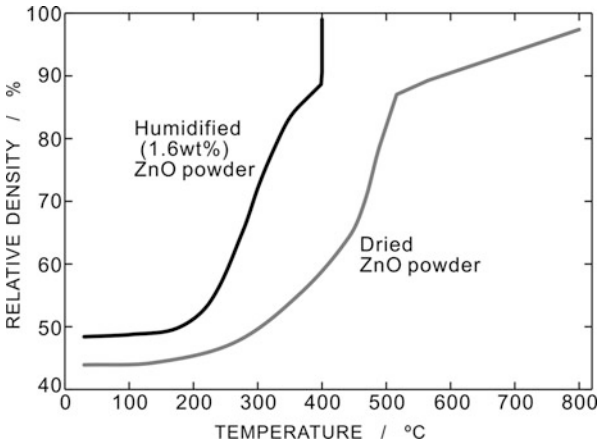

Fig. 14 Densification curves for humidified (1.6 wt%) and dried ZnO powder produced by SPS at a heating rate of 100 °C/min and maximum temperatures of 400 °C and 800 °C, respectively [149]

boundary may result into enhanced densification of ZnO at low temperatures. As mentioned in section "Role of Microstructure on Optical Properties," it is possible that some defect reactions would trigger enhanced diffusional mass transport and densification process in ECAS. The water-assisted ECAS/SPS will gain theoretical and practical importance in the future.

Flash Sintering

Flash sintering technique has received a lot of international attention in recent years as a drastic, almost instantaneous sintering process, which can be classified into ECAS. Raj and co-workers have demonstrated 3 mol% Y_2O_3-stabilized tetragonal ZrO_2 polycrystal (3Y-TZP) can be fully densified at 850 °C within 5 s under an electric field of 120 V/cm [151], while the same material can be usually densified by a conventional, pressureless sintering in air at 1400–1500 °C for several hours. The abrupt densification at relatively low sintering temperature is called flash sintering, in distinction from ECAS, in which the enhancement of densification is more gradual. Figure 15a shows typical setup of flash sintering experiment. A strong DC or AC electric field is applied to green compact by electric power supply through platinum wires. The furnace temperature, field strength, specimen current, and densification curve are schematically illustrated in Fig. 15b. The furnace temperature is raised at a constant heating rate. Beyond threshold field strength and furnace temperature, electric conductivity of the green compact abruptly increases, and electric current through the material accordingly increases. The almost instantaneous

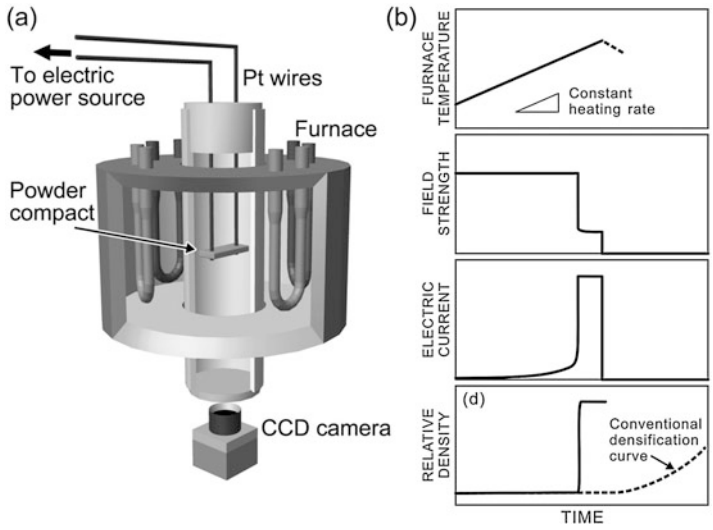

Fig. 15 (**a**) Typical setup of flash sintering experiment. (**b**) Schematics of furnace temperature, field strength, specimen current, and densification curve during flash sintering experiment

densification consequently takes place. The densification curves in 3Y-TZP sintered under different DC fields [151] as a function of furnace temperature are depicted in Figure 16. In this figure, the linear shrinkage data presented in ref. [151] were converted to relative density values. As shown in Fig. 16, abrupt densification of TZP occurred under the DC fields of higher than 60 V/cm, and the sintering temperature decreased with the increasing field strength. The flash sintering is characterized by almost immediate densification (typically occurs in just a few seconds) and a nonlinear increase in electric conductivity under a threshold condition of temperature and applied field [151, 152]. The nature of the flash sintering is fundamentally different from FAST, in which fields lead to a gradual enhancement in the sintering without any change in the specimen conductivity. Abrupt densification at low temperature by flash sintering has been demonstrated in various ceramics [153].

Flash sintering technique can be applied to various oxide and non-oxide ceramics, even low-sinterability materials such as Y_2O_3. For instance, DC fields greater than 300 V/cm can trigger the flash sintering in undoped Y_2O_3 [154]. Conventional sintering requires very high temperatures, typically $>$ 1600 °C as noted above, and a vacuum or hydrogen atmosphere. However, by applying an electric field of 1000 V/cm, for instance, a dense Y_2O_3 polycrystal was obtained at 985 °C in less than 10 s [154].

Nevertheless, full densification is still difficult to be accomplished by flash sintering. Typical example of the suppressed final density was seen in the flash sintering of $BaTiO_3$. Under a strong electric field beyond a critical value, flash sintering posed electric discharge damage in $BaTiO_3$ bodies, resulting in a low density of the sintered body with a number of residual pores and tunnellike

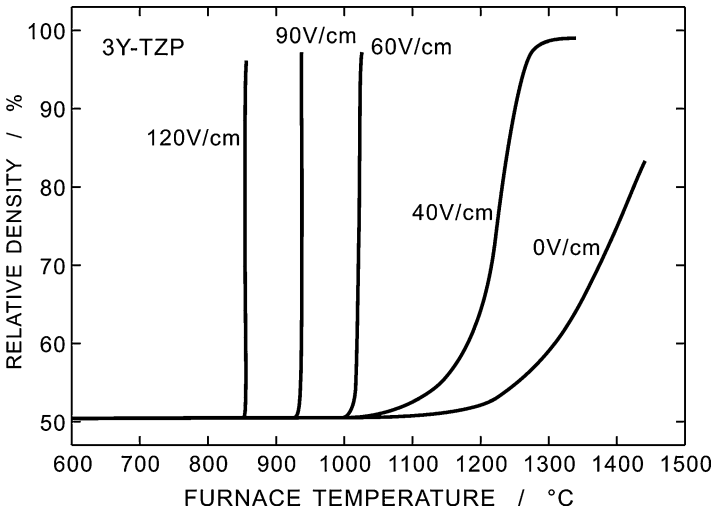

Fig. 16 The densification curves in 3Y-TZP sintered under different DC fields [151] as a function of furnace temperature

physical damages [155, 156]. In addition, crystalline thin layers were generated along $BaTiO_3$ grain boundaries in the vicinity of the electric discharged damage [157]. The Ba/Ti cation ratio of the secondary crystalline phases was Ti-excess, indicating that Ba cations tended to evaporate because of the excess heat yielded by the discharging.

EELS from grain boundaries and grain interiors in the flash-sintered materials revealed that the increased concentration of electric charge carriers was due to the excess oxygen vacancies generated by the electric fields; the changes in the fine structure of the Ti-L_{23} and O-K edges energy loss near edge structure (ELNES) were attributed to the excess oxygen vacancies. The excess oxygen vacancies induced by DC electric field was found to retard the sintering rate in the final sintering stage. Therefore, it is necessary to carefully control the specimen current for full densification of $BaTiO_3$ during flash sintering synthesis. In fact, by controlling current limit and heating schedule, more than 98% of theoretical density was obtained in $BaTiO_3$ by flash sintering [158]; for the electric current controlled flash sintering synthesis, the electric field of 100 V/cm with limiting current of 72 mA was applied up to 1070 °C, and then the electric field was switched off up to 1300 °C. The material manufactured by the current controlled flash sintering exhibited significantly fine-grained microstructure in comparison to that in conventionally sintered one.

At present, it is still difficult to produce transparent ceramics by flash sintering process. In addition, limited shape and dimensions of material are also disadvantages of flash sintering, as well as SPS so far. In contrast to the several disadvantages, flash sintering is a very attractive method because of the short sintering time and low sintering temperature, and the number of reports on flash sintering and related phenomena highly increases in recent years. It is expected to develop translucent or transparent ceramic bodies by flash sintering with short-time and low-temperature synthesis.

Concluding Remarks

Electric field/current-assisted sintering technology or spark plasma sintering is a versatile processing method for consolidation of various materials. Owing to the direct and rapid heating technology, SPS enables fully densified ceramic bodies consisting of nanoscale grains, which is ideally for achieving transparency of ceramic bodies. Moreover, by controlling the major sintering parameters, i.e., sintering temperature, isothermal sintering time, heating rate, and compressive pressure, transparent ceramics without residual pores can be manufactured by SPS technique, as briefly summarized in this chapter. Manufacturing of dense nanostructured body by SPS is also preferable to improve the mechanical properties of transparent ceramic materials. A number of studies have proven that ECAS/SPS synthesis is feasible for the production of transparent ceramic bodies, at least in the level of laboratory demonstrations.

Nevertheless, much fundamental research and development efforts are still required to use transparent ceramics produced by ECAS/SPS for industrial

applications. Fundamental investigations on the origin of enhanced densification in SPS are needed from atomistic point of view; a significant number of experimental results strongly indicated that some ionic defect reactions are involved during SPS processing. Effects of electrical current/field on mass transport, reactivity, microstructure evolution, and final chemical and physical properties are still remained to be understood. In order to control thermal and electrical conduction and stress distribution as well as mass transportation inside the die during SPS processing, new experimental techniques such as direct measurement of field strength inside a material and theoretical analyses such as FEM calculations must be employed.

On the other hand, for promoting transparent ceramics produced by SPS to industrial use, not only the improvement of physical/chemical properties but also upscaling of products and homogenization of microstructure are key technologies. Use of electro/magnetic fields pioneers new, unexpected technologies of ECAS/SPS. In addition, nanometer-scaled and defect-free microstructures attained by SPS not only improve mechanical strength but also enable superplastic deformation and near-net shape forming of the SPSed transparent ceramics. Scale up of components size and improvement in desirable properties of optically transparent ceramics through development of ECAS/SPS devices and progress in fundamental research on process will advance the industrial applications for the transparent ceramics in the near future.

References

1. Tokita M (2006) Am Ceram Soc Bull 85:32
2. Kodera Y, Hardin CL, Garay JE (2013) Scr Mater 69:149
3. Garay JE (2010) Annu Rev Mater Res 40:445
4. Grimm N, Scott GE, Sibold JD (1971) Ceram Bull 50:962
5. Hayashi K, Kobayashi O, Toyoda S, Morinaga K (1991) Mater Trans JIM 32:1024
6. O YT, Koo JB, Hong KJ, Park JS, Shin DC (2004) Mater Sci Eng A 374:191
7. Apetz R, van Bruggen PB (2003) J Am Ceram Soc 86:480
8. Lallemant L, Fantozzi G, Garnier V, Bonnefont G (2012) J Eur Ceram Soc 32:2909
9. Tokita M (1993) J Soc Powd Tech Jpn 30:790
10. Tamari N, Tanaka T, Tanaka K, Kondoh I, Kawahara M, Tokita M (1995) J. Ceram. Soc. Jpn 103:740
11. Perera DS, Tokita M, Moricca S (1998) J Eur Ceram Soc 18:401
12. Misawa T, Shikatani N, Kawakami Y, Enjoji T, Ohtsu Y, Fujita H (2009) J Mater Sci 44:1641
13. Orru R, Licheri R, Locci AM, Cincotti A, Cao G (2009) Mater Sci Eng R 63:127
14. Chaim R, Marder R, Estournes C (2010) Scr Mater 63:211
15. An LQ, Ito A, Goto T (2011) J Eur Ceram Soc 31:1597
16. Yang D, Conrad H (2010) Scr Mater 63:328
17. Yoshida H, Morita K, Kim B-N, Hiraga K, Yamanaka K, Soga K, Yamamoto T (2011) J Am Ceram Soc 94:3301
18. Anselmi-Tamburini U, Gennari S, Garay JE, Munir ZA (2005) Mater Sci Eng A 394:139
19. Bernard-Granger G, Guizard C (2007) Acta Mater 55:3493
20. Grasso S, Sakka Y, Maizza G (2009) Sci Technol Adv Mater 10:053001
21. Tokita M (2014) Ceram Jpn 49:91. (in Japanese)
22. Munir ZA, Quach DV, Ohyanagi M (2011) J Am Ceram Soc 94:1
23. Krell A, Blank P, Ma H, Hutzler T, Am J (2003) J Am Ceram Soc 86:12

24. Wei GC, Rhodes WH (2000) J Am Ceram Soc 83:1641
25. Mao XJ, Wang SW, Shimai S, Guo JK (2008) J Am Ceram Soc 91:3431
26. Shen ZJ, Johnsson M, Zhao Z, Nygren M (2002) J Am Ceram Soc 85:1921
27. Kim B-N, Hiraga K, Morita K, Yoshida H (2007) Scr Mater 57:607
28. Kim B-N, Hiraga K, Morita K, Yoshida H (2009) J Eur Ceram Soc 29:323
29. Kim B-N, Hiraga K, Morita K, Yoshida H, Miyazaki T, Kagawa Y (2009) Acta Mater 57:1319
30. Wang C, Zhao Z (2010) Mater Res Bull 45:1127
31. Penilla EH, Kodera Y, Garay JE (2013) Adv Funct Mater 23:6036
32. Wang SF, Zhang J, Luo DW, Gu F, Tang DY, Dong ZL, Tan GEB, Que WX, Zhang TS, Li S, Kong LB (2013) Prog Solid State Chem 41:20
33. Hou XR, Zhou SM, Jia TT, Lin H, Teng H (2011) Phys B Condens Matter 406:3931
34. Micheli AL, Dungan DF, Mantese JV (1992) J Am Ceram Soc 75:709
35. Iwasawa J, Nishimizu R, Tokita M, Kiyohara M, Uematsu K (2007) J Am Ceram Soc 90:2327
36. Saito N, Matsuda S, Ikegami T (1998) J Am Ceram Soc 81:2023
37. Zhang J, Wang S, An L, Liu M, Chen L (2007) J Lumin 122–123:8
38. Lefever RA, Matsko J (1967) Mater Res Bull 2:865
39. Majima K, Niimi N, Watanabe M, Katsuyama S, Nagai H (1993) J Alloys Compd 193:280
40. Ikesue A, Kamata K, Yoshida K (1996) J Am Ceram Soc 79:359
41. Serivalsatit K, Kokuoz B, Yazgan-Kokuoz B, Kennedy M, Ballato J (2010) J Am Ceram Soc 93:1320
42. Gan L, Park Y-J, Kim H, Kim J-M, Ko J-W, Lee J-W (2015) Ceram Int 41:9622
43. Hou XR, Zhou SM, Jia TT, Lin H, Teng H (2011) J Lumin 131:1953
44. Podowitz SR, Gaume R, Feigelson RS (2010) J Am Ceram Soc 93:82
45. An LQ, Ito A, Goto T (2012) J Eur Ceram Soc 32:1035
46. Yoshida H, Morita K, Kim B-N, Hiraga K, Kodo M, Soga K, Yamamoto T (2008) J Am Ceram Soc 91:1707
47. Zhang HB, Kim B-N, Morita K, Yoshida H, Hiraga K, Sakka Y (2011) J Am Ceram Soc 94:3206
48. Yoshida H, Morita K, Kim B-N, Soga K, Yamamoto T (2018) J Eur Ceram Soc 38:1972
49. Garvie RC, Hannink RH, Pascoe RT (1975) Nature 258:703
50. Matsui K, Yoshida H, Ikuhara Y (2018) Int Mater Rev 63:375
51. Mazdiyasni KS, Lynch CT, Smith JS II (1967) J Am Ceram Soc 50:532
52. Tsukuma K, Yamashitaw I, Kusunose T (2008) J Am Ceram Soc 91:813
53. Peuchert U, Okano Y, Menke Y, Reichel S, Ikesue A (2009) J Eur Ceram Soc 29:283
54. Tsukuma K (1986) J Mater Sci Lett 5:1143
55. Casolco SR, Xu J, Garay JE (2008) Scr Mater 58:516
56. Anselmi-Tamburini U, Woolman JN, Munir ZA (2007) Adv Funct Mater 17:3267
57. Zhang H, Kim B-N, Morita K, Yoshida H, Lim J-H, Hiraga K (2011) J Am Ceram Soc 94:2981
58. Klimke J, Trunec M, Krell A (2011) J Am Ceram Soc 94:1850
59. Ikegami T, Matsuda SI, Suzuki H (1974) J Am Ceram Soc 57:507
60. Chen D, Jordan EH, Gell M (2008) Scr Mater 59:757
61. Suzuki M, Ikegami T, Yokoyama M, Komatsu T, Fukahori A (2005) J Ceram Soc Jpn 113:149
62. Vasilos T, Spriggs RM (1963) J Am Ceram Soc 46:493
63. Vieira JM, Brook RJ (1984) J Am Ceram Soc 67:450
64. Ehre D, Gutmanas EY, Chaim R (2005) J Eur Ceram Soc 25:3579
65. Itatani K, Tsujimoto T, Kishimoto A (2006) J Eur Ceram Soc 26:639
66. Benecke MW, Olson NE, Pask JA (1967) J Am Ceram Soc 50:365
67. Fang Y, Agrawal D, Skandan G, Jain M (2004) Mater Lett 58:551
68. Kan A, Moriyama T, Takahashi S, Ogawa H (2011) Jpn J Appl Phys 50:09NF2
69. Rhodes WH, Sellers DJ (1967) Am Ceram Soc Bull 46:469
70. Hart PE, Pask JA (1971) J Am Ceram Soc 54:315
71. Chaim R, Shen ZJ, Nygren M (2004) J Mater Res 19:2527
72. Tran TB, Hayun S, Navrotsky A, Castro RHR (2012) J Am Ceram Soc 95:1185

73. Liu J, Fu ZY, Wang WM, Zhang JY, Wang H, Wang YC, Lee SW, Niihara K (2014) J Eur Ceram Soc 34:3095–3102
74. Jiang N, Xie R-J, Liu Q, Li J (2017) J Eur Ceram Soc 37:4947
75. Ganesh I (2013) Int Mater Rev 58:63
76. Ting C-J, Lu H-Y (2000) J Am Ceram Soc 83:1592
77. du Merac MR, Reimanis IE, Kleebe H-J (2015) J Am Ceram Soc 98:2130
78. Chiang Y-M, Kingery WD (1989) J Am Ceram Soc 72:271
79. Ting CJ, Lu HY (1999) Acta Mater 47:817
80. Reimanis IE, Kleebe HJ (2009) J Am Ceram Soc 92:1472
81. Wang CT, Lin LS, Yang SJ (1992) J Am Ceram Soc 75:2240
82. Bhaduri S, Bhaduri SB (2002) Ceram Int 28:153
83. Goldstein A, Goldenberg A, Yeshurun Y, Hefetz M (2008) J Am Ceram Soc 91:4141
84. Biswas P, Rajeswari K, Ramavath P, Johnson R, Maiti HS (2013) J Am Ceram Soc 96:3042
85. Rodríguez EA, Castillo G-A, Das TK, Puente-Ornelas R, González Y, Arato A-M, Aguilar-Martínez JA (2013) J Eur Ceram Soc 33:2767
86. Li J-H, Cai B-Y, Feng W-W, Liu Y-Q, Ma H-W (2013) Ceram Int 39:8393
87. Gehre P, Aneziris CG, Berek H, Parr C, Reinmöller M (2015) J Eur Ceram Soc 35:1613
88. Frage N, Cohen S, Meir S, Kalabukhov S, Dariel MP (2007) J Mater Sci 42:3273
89. Morita K, Kim BN, Hiraga K, Yoshida H (2009) J Am Ceram Soc 92:1208
90. Muche DNF, Drazin JW, Mardinly J, Deya S, Castro RHR (2017) Mater Lett 186:298
91. Morita K, Kim B-N, Yoshida H, Hiraga K, Sakka Y (2015) Acta Mater 84:9
92. Morita K, Kim B-N, Yoshida H, Hiraga K, Sakka Y (2018) J Eur Ceram Soc 38:2596
93. Xu GG, Zhang XD, He W, Liu H, Li H (2006) Mater Lett 60:962
94. Ikesue A, Furusato I, Kamata K (1995) J Am Ceram Soc 78:225
95. Lee HD, Mah TI, Parthasarathy TA (2008) Low-cost processing of fine grained transparent yttrium aluminum garnet. In: 28th international conference on advanced ceramics and composites a: ceramic engineering and science proceedings, vol 25, p 147
96. Zych E, Brecher C (2000) J Lumin 90:89
97. Chaim R, Kalina M, Shen JZ (2007) J Eur Ceram Soc 27:3331
98. Frage N, Kalabukhov S, Sverdlov N, Ezersky V, Dariel MP (2010) J Eur Ceram Soc 30:3331
99. Spina G, Bonnefont G, Palmero P, Fantozzi G, Chevalier J, Montanaro L (2012) J Eur Ceram Soc 32:2957
100. Doremus RH (1992) J Mater Sci 27:285
101. Dorozhkin SV (2010) Biomaterials 31:1465
102. Takikawa K, Akao M (1996) J Mater Sci Mater Med 7:439
103. Kotobuki N, Ioku K, Kawagoe D, Fujimore H, Goto S, Ohgushi H (2005) Biomaterials 26:779
104. John A, Varma HK, Vijayan S, Bernhardt A, Lode A, Vogel A, Burmeister B, Hanke T, Domaschke H, Gelinsky M (2009) Biomed Mater 4:015007. (9pp)
105. Ioku K, Yosimura M, Somiya S (1988) J. Ceram. Soc. Japan 96:109
106. Wang J, Shaw LL (2010) Scr Mater 63:593
107. Uematsu K, Takagi M, Honda T, Uchida N, Saito K (1989) J Am Ceram Soc 72:1476
108. Fang Y, Agrawal DK, Roy DM, Roy R (1995) Mater Lett 23:147
109. Eriksson M, Liu Y, Hu J, Gao L, Nygren M, Shen Z (2011) J Eur Ceram Soc 31:1533
110. Kim B-N, Prajatelistia E, Han Y-H, Son H-W, Sakka Y, Kim S (2013) Scr Mater 69:366
111. Yoshida H, Kim B-N, Son H-W, Han Y-H, Kim S (2013) Scr Mater 69:155
112. Cheng JP, Agrawal D, Zhang YJ, Roy R (2000) J Mater Sci Lett 20:77
113. Yuan XY, Liu XJ, Zhang F, Wang SW (2010) J Am Ceram Soc 93:22
114. Yuan XY, Zhang F, Liu XJ, Zhang Z, Wang SW (2011) J Inorg Mater 26:499
115. Zientara D, Bucko MM, Lis J (2007) J Eur Ceram Soc 27:4051
116. Kumar RS, Rajeswari K, Praveen B, Hareesh UNS, Johnson R (2010) J Am Ceram Soc 93:429
117. Chen F, Zhang F, Wang J, Zhang HL, Tian R, Zhang J, Zhang Z, Sun F, Wang SW (2014) Scr Mater 81:20
118. Sahin FC, Kanbur HE, Apak B (2012) J Eur Ceram Soc 32:925

119. Li X, Luo J, Zhou Y (2015) J Eur Ceram Soc 35:2027
120. Shan Y, Wei Z, Sun Z, Xu J, Qin Q, Olevsky EA (2017) J Mater Res 32:3279
121. Nakanishi Y (1984) J Mater Sci Lett 3:471
122. Kuramoto N, Taniguchi H, Aso I (1986) IEEE Trans Compon 9:386
123. Kuramoto N, Taniguchi H, Aso I (1989) Am Ceram Soc Bull 68:883
124. Kuramoto N, Taniguchi H (1984) J Mater Sci Lett 3:471
125. Xiang M, Zhou Y, Xu W, Li X, Wang K, Pan W (2018) J Ceram Soc Jpn 126:241
126. Baranda PS, Knudsen AK, Ruh E (1993) J Am Ceram Soc 76:1751
127. Watari K, Hwang HJ, Toriyama M, Kanzaki S (1999) J Mater Res 14:1409
128. Panchula ML, Ying JY (2003) J Am Ceram Soc 86:1121
129. Jarrige J, Lecompte JP, Mullo J, Müller G (1997) J Eur Ceram Soc 17:1891
130. He XL, Ye F, Zhang HJ, Zhou ZQ (2010) Mater Des 31:4110
131. He X, Ye F, Liu LM, Zhang HJ (2011) Mater Sci Technol 27:513
132. Nishimura T, Sekine K, Yamamoto Y, Hirosaki N, Ishigaki T (2010) J Ceram Soc Jpn 118:1050
133. Fu ZY, Liu JF, Wang H, He DH, Zhang QJ (2004) Mater Sci Technol 20:1097
134. Kojima K, Okada G, Fukuda K, Yanagida T (2016) Radiat Meas 94:78
135. Chen Y, Zhang L, Zhang J, Liu P, Zhou T, Zhang H, Gong D, Tang D, Shen D (2015) Opt Mater 50:36
136. Li Y, Wu Y (2015) J Am Ceram Soc 98:2972
137. Chen S, Wu Y (2013) Am Ceram Soc Bull 92:32
138. Chlique C, Merdrignac-Conanec O, Hakmeh N, Zhang X, Adam JL (2013) J Am Ceram Soc 96:3070
139. McCloy JS, Tustison RW (2013) Chemical vapor deposited zinc sulfide. SPIE Press, Bellingham
140. Karaksina EV, Ikonnikov VB, Gavrishchuk EM (2007) Inorg Mater 43:452
141. Chlique C, Delaizir G, Merdrignac-Conanec O, Roucau C, Dollé M, Rozier P, Bouquet V, Zhang X (2011) Opt Mater 33:706
142. Chen I-W, Wang X-H (2000) Nature 404:168
143. Grasso S, Hu CF, Maizza G, Kim B-N, Sakka Y (2011) J Am Ceram Soc 94:1405
144. Boulesteix R, Maitre A, Lemanski K, Deren PJ (2017) J Alloys Compd 722:358–364
145. Schwarz S, Guillon O (2013) J Eur Ceram Soc 33:637
146. Zgalat-Lozynskyy O, Herrmann M, Ragulya A (2011) J Eur Ceram Soc 31:809
147. Guillon O, Gonzalez-Julian J, Dargatz B, Kessel T, Schierning G, Räthel J, Herrmann M (2014) Adv Eng Mater 16:830
148. Schwarz S, Thron AM, Rufner J, van Benthem K, Guillon O (2012) J Am Ceram Soc 95:2451
149. Dargatz B, Gonzalez-Julian J, Bram M, Jakes P, Besmehn A, Schade L, Röder R, Ronning C, Guillon O (2016) J Eur Ceram Soc 36:1207
150. Nie J, Zhang Y, Chan JM, Huang R, Luo J (2018) Scr Mater 142:79
151. Cologna M, Rashkova B, Raj R (2010) J Am Ceram Soc 93:3556
152. Raj R, Cologna M, Francis JSC (2011) J Am Ceram Soc 94:1941
153. Dancer CFJ (2016) Mater Res Express 3:102001
154. Yoshida H, Sakka Y, Yamamoto T, Lebrun J-M, Raj R (2014) J Eur Ceram Soc 34:991
155. M'Peko JC, Francis JSC, Raj R (2014) J Eur Ceram Soc 34:3655
156. Uehashi A, Yoshida H, Tokunaga T, Sasaki K, Yamamoto T (2015) J Ceram Soc Jpn 123:465
157. Yoshida H, Uehashi A, Tokunaga T, Sasaki K, Yamamoto T (2016) J Ceram Soc Jpn 124:388
158. Nakagawa Y, Yoshida H, Uehashi A, Tokunaga T, Sasaki K, Yamamoto T (2017) J Am Ceram Soc 100:3843